Human Molecular Genetics, 2014, Vol. 23, No. 5 ***1134–1150***
doi:10.1093/hmg/ddt508
Advance Access published on October 9, 2013

Connexin defects underlie arrhythmogenic right ventricular cardiomyopathy in a novel mouse model

Robert C. Lyon[1,†], Valeria Mezzano[1,†], Adam T. Wright[2], Emily Pfeiffer[2], Joyce Chuang[2], Katherine Banares[1], Allan Castaneda[1], Kunfu Ouyang[1], Li Cui[3], Riccardo Contu[1], Yusu Gu[1], Sylvia M. Evans[3], Jeffrey H. Omens[1,2], Kirk L. Peterson[1], Andrew D. McCulloch[2] and Farah Sheikh[1,*]

[1]Department of Medicine, [2]Department of Bioengineering, [3]Department of Skaggs School of Pharmacy, University of California-San Diego, 9500 Gilman Drive, La Jolla, CA 92093, USA

Received July 30, 2013; Revised September 6, 2013; Accepted October 4, 2013

Arrhythmogenic right ventricular cardiomyopathy (ARVC) termed a 'disease of the desmosome' is an inherited cardiomyopathy that recently underwent reclassification owing to the identification of left-dominant and biventricular disease forms. Homozygous loss-of-function mutations in the desmosomal component, desmoplakin, are found in patients exhibiting a biventricular form of ARVC; however, no models recapitulate the postnatal hallmarks of the disease as seen in these patients. To gain insights into the homozygous loss-of-function effects of desmoplakin in the heart, we generated cardiomyocyte-specific desmoplakin-deficient mice (DSP-cKO) using ventricular myosin light chain-2-Cre mice. Homozygous DSP-cKO mice are viable but display early ultrastructural defects in desmosomal integrity leading to a cardiomyopathy reminiscent of a biventricular form of ARVC, which includes cell death and fibro-fatty replacement within the ventricle leading to biventricular dysfunction, failure and premature death. DSP-cKO mice also exhibited ventricular arrhythmias that are exacerbated with exercise and catecholamine stimulation. Furthermore, DSP-cKO hearts exhibited right ventricular conduction defects associated with loss of connexin 40 expression and electrical wavefront propagation defects associated with loss of connexin 43 expression. Dose-dependent assessment of the effects of loss of desmoplakin in neonatal ventricular cardiomyocytes revealed primary loss of connexin 43 levels, phosphorylation and function independent of the molecular dissociation of the mechanical junction complex and fibro-fatty manifestation associated with ARVC, suggesting a role for desmoplakin as a primary stabilizer of connexin integrity. In summary, we provide evidence for a novel mouse model, which is reminiscent of the postnatal onset of ARVC while highlighting mechanisms underlying a biventricular form of human ARVC.

INTRODUCTION

Arrhythmogenic right ventricular cardiomyopathy (ARVC) is an inherited cardiac muscle disease that is associated with a high frequency of ventricular arrhythmias leading to sudden cardiac death in young children and adults including athletes (1). Compelling evidence from human genetic studies and genetic mouse models has linked ARVC to genetic deficiencies in components of the desmosomes, which are specialized cell–cell junctions within cardiac muscle (2–11). Desmosomes are composed of transmembrane desmosomal cadherins (desmocollin 2 and desmoglein 2), armadillo proteins [plakoglobin (γ-catenin) and plakophilin 2] and the centralized plakin protein, desmoplakin, which links the junctional complex to the intermediate filament, desmin, to maintain mechanical integrity of cardiac muscle (12). Desmoplakin was the first desmosomal gene linked to autosomal dominant ARVC following the identification of a missense mutation in desmoplakin in a family of Italian descent harboring ARVC (3). These patients exhibited right ventricular dilatation and arrhythmias, causing sudden cardiac death in some of the family members (3). Both dominant and recessive ARVC-associated desmoplakin mutations have been identified in

*To whom correspondence should be addressed at: Department of Medicine (Cardiology Division), University of California-San Diego, 9500 Gilman Drive, La Jolla, CA 92093-0613C, USA. Tel: +858 2460754; Fax: +858 8221355; Email fasheikh@ucsd.edu
†The authors wish it to be known that, in their opinion, the first two authors contributed equally to this work and should be regarded as joint first authors.

humans (3,13–16), one of which is a homozygous loss of function mutation that causes truncation and loss of the major cardiac isoform of desmoplakin (13). However, current mouse models targeting loss or mutations in desmoplakin (7,10,17) do not recapitulate the postnatal severity and pathogenic hallmarks of the disease as seen in patients with homozygous loss of function mutations in desmoplakin (13).

Although genetic mouse models harboring heterozygous loss or mutations in desmosomal genes (7–11,17,18), including desmoplakin, have paved the way to better understanding the pathophysiology of ARVC, there remain a number of open questions regarding the manifestation of the disease features and mechanisms ascribed to the postnatal onset of ARVC. For instance, fibro-fatty replacement of the ventricle is considered a hallmark of ARVC and has been widely postulated to be a key pathological factor that elicits the fatal arrhythmias; however, it is yet to be determined whether there is a direct and early mechanistic consequence of desmosomal (e.g. desmoplakin) deficiency on gap junction components and cell–cell coupling in a system independent of the fibro-fatty manifestation. This is important to determine because a recent study suggested that electrophysiological abnormalities were thought to appear prior to fibro-fatty replacement of the myocardium in human ARVC patients carrying desmoplakin mutations and heterozygous desmoplakin-deficient mice (19). Adding to the complexity of identifying common mechanisms underlying the pathogenesis of ARVC is the recent discovery of complex and heterogeneous disease patterns for ARVC, which not only include the classic right ventricle-dominant form but also left ventricle-dominant and biventricular (parallel involvement of both ventricles) forms, which have led to including the adopted term, arrhythmogenic cardiomyopathy to reference this class of diseases (20). The discovery of left ventricle-dominant and biventricular forms of ARVC arose partly from the reevaluation of previously diagnosed patients exhibiting dilated cardiomyopathy, which were now shown to exhibit classic features of ARVC, such as tachyarrhythmias (20). These observations help to not only explain the identification of desmosomal mutations in dilated cardiomyopathy patients (21) but also offer insights into the complex disease presentation of ARVC among different patients (22). Recent studies have linked mutations in the desmosomal gene, desmoplakin, to patients primarily exhibiting left ventricular-dominant and biventricular forms of ARVC (22–24), highlighting the need to reevaluate molecular mechanisms (loss of junctional plakoglobin) and pathological (fatty deposition) hallmarks in these new settings. This would be important to determine because a current theory suggests that loss of junctional plakoglobin and its nuclear translocation following desmosomal disruption is thought to suppress canonical Wnt/β-catenin signaling to drive adipogenesis specifically in secondary (right) heart field progenitor cells (7,25,26). Furthermore, there is clinical and histological evidence of fibro-fatty replacement in the left ventricle in 47–76% of ARVC cases (27,28). Loss of plakoglobin from the cardiac muscle cell–cell junction has also been proposed as a potential marker for ARVC (29); however, recent studies suggest that not all patients display loss of junctional plakoglobin (30), highlighting that there may be human ARVC subpopulations that exhibit distinct molecular hallmarks associated with ARVC disease pathogenesis. Thus, developing genetic mouse models, which distinguish the postnatal onset of these forms of ARVC, could serve as important tools to help uncover mechanisms that commonly and specifically underlie these disease subtypes as well as a platform to uncover specific treatment modalities.

In the current study, we present a novel mouse model of ARVC that is reminiscent of the postnatal onset of a biventricular form of human ARVC at the histological, physiological and electrophysiological levels. We identify the cellular origin of a specific region of the fatty deposition in DSP-cKO hearts by showing that subepicardial fat deposition originates from a cardiac muscle lineage and that the mechanisms are independent of junctional loss of plakoglobin as we show retained plakoglobin at cell–cell junctions in DSP-cKO hearts. We also provide evidence for desmoplakin as a direct stabilizer of connexin integrity, which includes the demonstration that loss of desmoplakin has direct mechanistic consequences on connexin 43 levels and phosphorylation, leading to conduction abnormalities prior to the molecular dissociation of the mechanical junction complex within a system that is independent of the fibro-fatty manifestation observed in ARVC.

RESULTS

Characterization of cardiomyocyte-specific desmoplakin knockout mice

To determine the homozygous loss-of-function effects of desmoplakin in the heart, desmoplakin-floxed mice ($DSP^{flox/flox}$) were crossbred with the well-established cardiomyocyte-specific ventricular myosin light chain-2-Cre recombinase (MLC2v-Cre) knock-in mice (31–34). A breeding strategy was utilized to generate ventricular cardiomyocyte-specific homozygous DSP-cKO [$DSP^{flox/flox}$:$MLC2v^{Cre(+)}$], heterozygous DSP-cKO [$DSP^{flox/+}$:$MLC2v^{Cre(+)}$] as well as littermate controls [$DSP^{flox/flox}$:$MLC2v^{Cre(-)}$] (Fig. 1A). Homozygous DSP-cKO were viable and born at expected Mendelian ratios (data not shown); however, they displayed a striking susceptibility to postnatal lethality from the age of 1 month onwards (Fig. 1B). Kaplan–Meier survival analyses of litters revealed that 50% of homozygous DSP-cKO mice die within 2 months of age, eventually resulting in 100% mortality by the age of 5 months compared with littermate controls (Fig. 1B) as well as heterozygous DSP-cKO mice, which display no mortality at this stage (data not shown). As a result, all subsequent studies on DSP-cKO mice were performed on homozygous DSP-cKO mice, which were designated as DSP-cKO.

To determine the efficiency of desmoplakin knock-down in DSP-cKO hearts *in vivo,* we assessed desmoplakin protein expression in purified ventricular cardiomyocytes from DSP-cKO and littermate control hearts at 3 weeks of age. A significant $83 \pm 5.6\%$ ($n = 3$) and $87 \pm 4.3\%$ ($n = 3$) reduction in desmoplakin protein levels was observed in both total and insoluble (intercalated disc-enriched) fractions, respectively, in DSP-cKO cardiomyocytes when compared with littermate controls (Fig. 1C). Immunofluorescence staining analyses of cardiac sections highlighted the dramatic loss of desmoplakin within intact intercalated discs (white arrows), which is delineated by the retained presence of N-cadherin, in DSP-cKO hearts, when compared with littermate hearts (Fig. 1D). The retained desmoplakin expression in DSP-cKO cardiac sections could either reflect retained

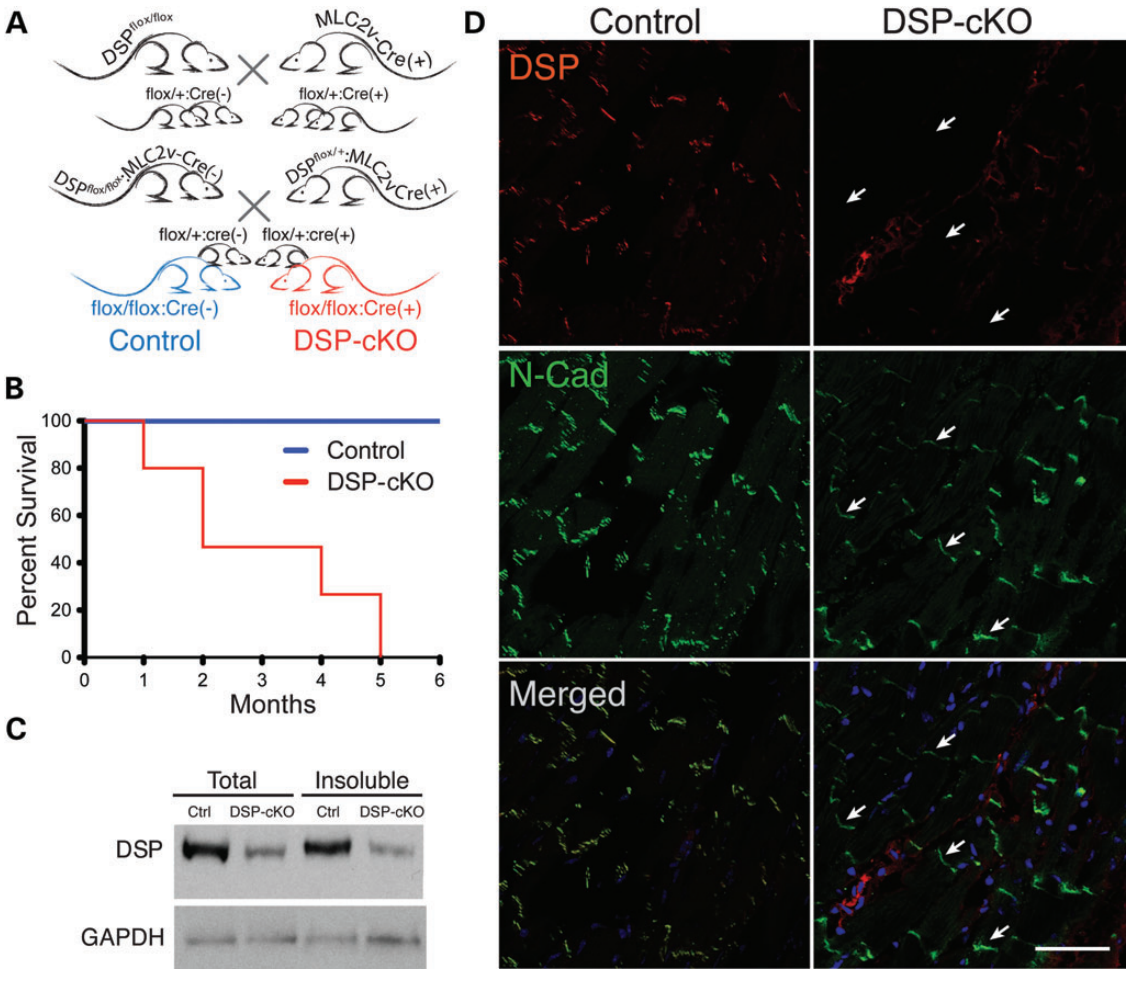

Figure 1. Generation, survival and desmoplakin expression analysis of DSP-cKO mice. (**A**) Schematic representation of breeding strategy to generate DSP-cKO [$DSP^{flox/flox}$:$MLC2v^{Cre(+)}$] and littermate control [$DSP^{flox/flox}$:$MLC2v^{Cre(-)}$] mice. (**B**) Kaplan–Meier survival curve analysis of control ($n = 15$) and DSP-cKO ($n = 15$) mice from birth. (**C**) Ventricular cardiomyocytes were isolated from DSP-cKO and littermate control hearts at 3 weeks of age. Desmoplakin expression in DSP-cKO and control cardiomyocytes was assessed in both total and insoluble protein extracts using specific antibodies to desmoplakin and GAPDH (loading control). (**D**) Immunofluorescence staining of desmoplakin in cardiac sections from representative DSP-cKO and littermate control mice at 4 weeks of age. Cardiac sections were double-labeled with antibodies against desmoplakin (red) and N-cadherin (green), as well as being counterstained with DAPI nuclear stain (blue). White arrows highlight areas where there is specific loss of desmoplakin within intact intercalated discs in DSP-cKO hearts (denoted by the presence of N-cadherin). Bar represents 9 μm.

desmoplakin expression in cardiomyocytes not targeted by MLC2v-Cre (as it is not 100% efficient). It could also reflect desmoplakin expression in non-muscle cells, because desmoplakin expression is also reported in non-muscle cell types (e.g. endothelial cells) (35).

DSP-cKO hearts display early ultrastructural defects in desmosomal integrity

As desmoplakin is localized to the desmosomes within the intercalated disc, transmission electron microscopy was performed on DSP-cKO mouse hearts to examine the integrity of these structures at the ultrastructural level. Representative micrographs from DSP-cKO hearts (Fig. 2C and D) revealed specific defects in intercalated disc integrity as early as 2.5 weeks, which included rupture of desmosomes and loss of myocyte–myocyte adhesion between neighboring cells, as evidenced by the intercellular gaps, when compared with littermate control hearts (Fig. 2A and B). Similar ultrastructural findings have been observed in human skin of patients with DSP mutations and human hearts from ARVC patients (36,37). It should be noted that in very severely affected regions, DSP-cKO hearts also displayed some loss of muscle architecture coupled with the observed adhesion defects as evidenced by the intercellular gaps being associated with loss or thickening of Z-lines (Fig. 2C and D). These results altogether suggest that defects in desmosomal structural integrity is one of the primary causes of dysfunction in this model.

DSP-cKO mice display a severe form of ventricular cardiomyopathy similar to a biventricular form of arrhythmogenic right ventricular cardiomyopathy

To evaluate whether DSP-cKO mice recapitulate key clinical features of human ARVC, we performed morphological, immunohistochemical and functional analyses of DSP-cKO versus

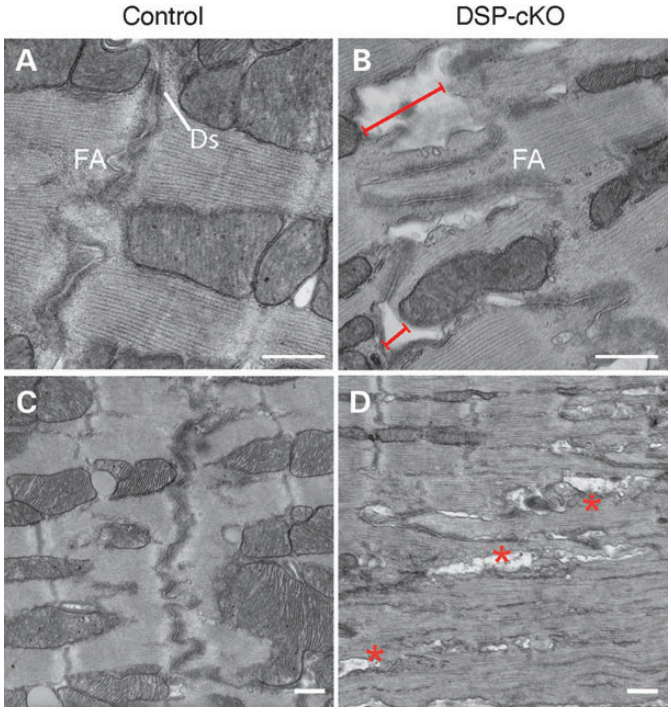

Figure 2. Ultrastructural analysis of DSP-cKO mouse hearts. Representative transmission electron micrographs from the ventricular myocardium of control (**A** and **C**) and DSP-cKO (**B** and **D**). Red bars highlight the loss of attachment between plasma membranes of the adjacent cells. Red asterisks denote areas with complete breakdown of the intercalated disc structures. Ds, desmosome; FA, fascia adherens junction. Bar represents 500 nm.

littermate control hearts. At 4 weeks of age, morphological analyses of DSP-cKO hearts revealed that they were grossly enlarged in size, when compared with littermate controls (Fig. 3A). Further histological analyses at this age showed that DSP-cKO mice displayed significant right and left ventricular chamber dilation when compared with controls; however, it was evident that the extent of dilation and wall thinning was more pronounced in the right ventricle (Fig. 3B). DSP-cKO hearts also displayed extensive fibrosis, which could be detected in the right and left ventricles as well as septum (Fig. 3C). However, the effects on fibrosis were exclusive to the ventricular chambers as no fibrosis could be detected in the enlarged atria of DSP-cKO hearts, similar to controls (Fig. 3C). DSP-cKO hearts also displayed an increase in TUNEL-positive cells, which was found in the cardiac mid-wall but more pronounced in the subepicardial region of the heart (Supplementary Material, Fig. S1), suggesting that apoptotic cell death is a contributing factor to the massive increase in collagen deposition. Oil Red O staining of cardiac sections from DSP-cKO right hearts at 6 weeks of age further revealed pronounced pockets of fat deposition within the subepicardium (Fig. 3D). Punctate staining of Oil Red O could also be observed in the mid-wall region of DSP-cKO hearts (Fig. 3D), suggesting that there is a gradient of fat deposition decreasing toward the endocardium. Similar patterns of fibro-fatty deposition have been reported in human hearts from ARVC patients (27). These features of fatty deposition were also observed in the left ventricle of DSP-cKO hearts (data not shown). Fat deposition could not be detected in control hearts (Fig. 3D). To determine the cellular origin of the fat deposition in DSP-cKO hearts at postnatal stages, homozygous DSP-cKO mice were cross-bred with Cre-inducible R26RtdTomato reporter mice (38), to generate $DSP^{flox/flox}$:$MLC2v^{Cre(+)}$:$R26^{RtdTomato}$ mice (Fig. 3E). R26RtdTomato reporter mice specifically express Tomato Red (TomRed) when exposed to Cre recombinase. Thus, expression of TomRed in the background of $DSP^{flox/flox}$:$MLC2v^{Cre(+)}$ mice genetically marks all MLC2v-positive (+) cells in this model, from the earliest stage when MLC2vCre is active (embryonic day 7.75) (34), thus marking cells of a cardiomyocyte muscle lineage (Fig. 3E). Similar to Oil Red O staining results, we show that DSP-cKO hearts contain two pools of lipid-positive cells. We show strong co-localization of perilipin, a marker of mature lipid droplets, with TomRed, specifically within the subepicardial layer of postnatal DSP-cKO hearts (Fig. 3F), suggesting that the subepicardial fat deposition in DSP-cKO hearts originates from a cardiac muscle lineage. However, our studies also show that punctate perilipin staining could also be observed in cells within the mid-wall that are TomRed negative (Fig. 3F), suggesting that non-muscle cells may also contribute to the lipid deposition observed in DSP-cKO hearts.

To determine how the morphological and histological defects in DSP-cKO hearts impact cardiac function, we utilized a non-invasive magnetic resonance imaging (MRI) technique to simultaneously measure right and left ventricular dimensions, wall thickness and function (39). This is important because the crescentic shape and size of the right ventricle has provided challenges in its imaging as well as reliable functional assessment in the mouse using echocardiography (40). To determine the feasibility of MRI as a method to simultaneously assess anatomical changes in the left and especially right ventricle in a mouse model of heart disease, we obtained a series of MRI (short axis) images at end-diastole and end-systole and, from the segmented endocardial borders, created three-dimensional (3D) biventricular models of each heart (Fig. 4A). Despite the unique shape and size of the right ventricle, we provide evidence of the feasibility of using 3D reconstruction methods to accurately quantify the extensive remodeling in DSP-cKO hearts, as evidenced by the enlargement and extension of the right ventricle over the left ventricle (Fig. 4A). These anatomical changes were reflective of the gross morphological changes observed in DSP-cKO versus control hearts via histology (Fig. 3B). Assessment of right and left ventricular end-diastolic and end-systolic volumes, as well as ejection fraction was subsequently performed on DSP-cKO and littermate control mice. Representative long-axis MRI images from DSP-cKO versus littermate control hearts at end-systole further highlight the abnormalities in right and left ventricular dimensions in DSP-cKO mice (Fig. 4B). No significant changes in heart rate and body weight were observed in DSP-cKO mice when compared with littermate controls at this stage. However, DSP-cKO hearts displayed significantly (i) increased end-diastolic and end-systolic volumes, (ii) reduced ejection fraction as well as (iii) reduced wall thickness in both the right and left ventricle when compared with littermate controls (Fig. 4C). The significant changes in cardiac dimensions, wall thickness and function in DSP-cKO hearts were indicative of biventricular dilation and depressed systolic function. These results show that the DSP-cKO model recapitulates cardiac features similar to a form of ARVC where both right and left

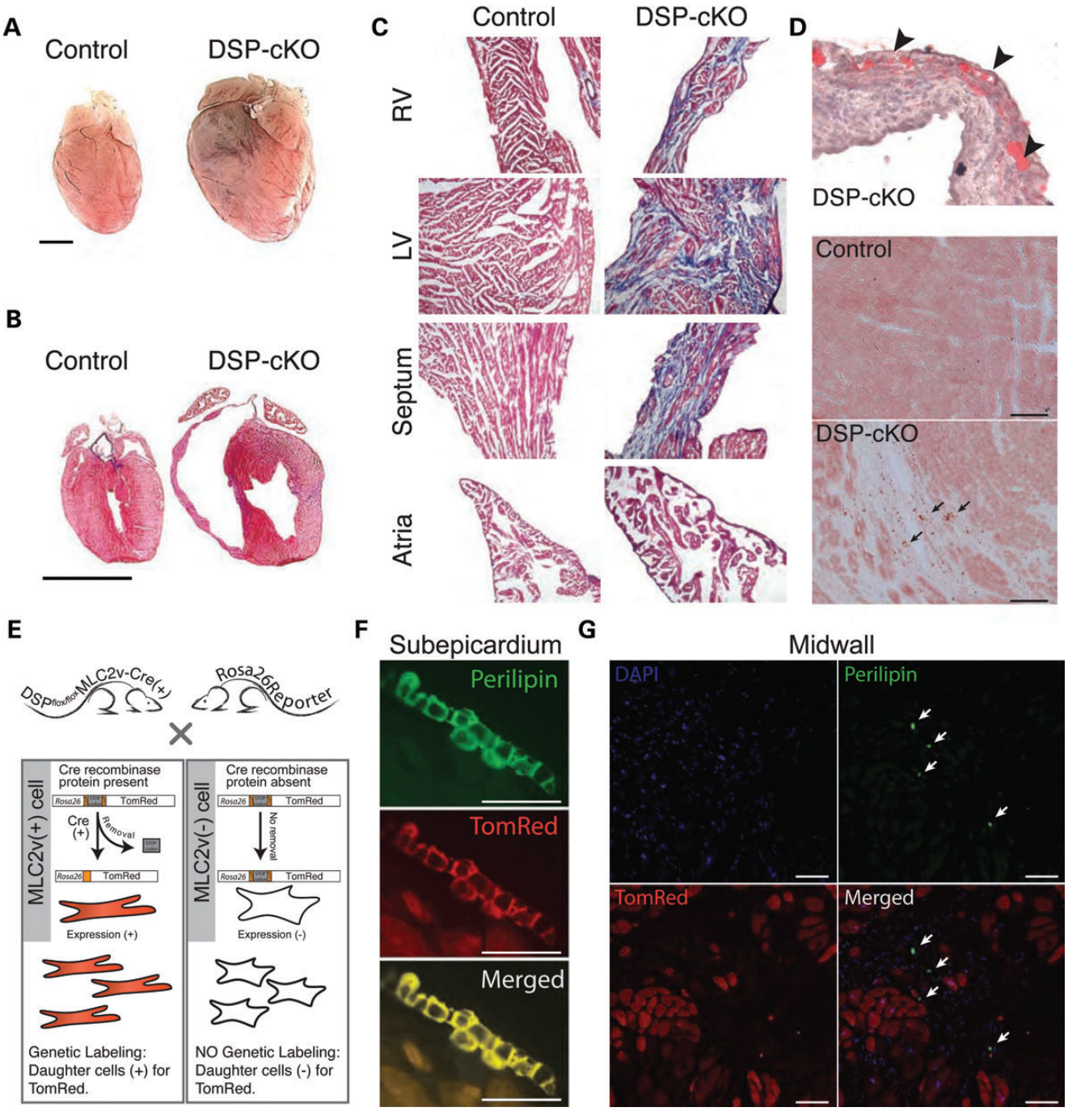

Figure 3. Histological analysis of DSP-cKO mice. (**A**) Whole-heart and (**B**) cardiac sections from DSP-cKO and control mice at 4 weeks. Sections were stained for nuclei and cytoplasm with hematoxylin and eosin, respectively. Bars in A and B represent 2 and 0.67 mm, respectively. (**C**) Masson trichrome stain of DSP-cKO and control mouse heart sections at 4 weeks. Bar represents 100 μm. (**D**) Oil Red O staining of DSP-cKO and control mouse heart (upper panel: RV free-wall; lower panels: RV myocardium) sections at 6 weeks. Arrowheads and arrows indicate regions of fat deposition. Bar in lower panels represents 100 μm. (**E**) Schematic representation of the mating strategy used to generate mice with TomRed reporter in the background of $DSP^{flox/flox}$:$MLC2v^{Cre(+)}$ mice for lineage tracing experiments to seek origin of fat deposition. (**F**) Immunofluorescence staining of perilipin in subepicardial layer of cardiac sections of DSP-cKO mice. (**G**) Immunofluorescence staining of perilipin in mid-wall region of cardiac sections of DSP-cKO mice. For F and G, cardiac sections were labeled with an antibody against perilipin (green) as well as being counter-stained with DAPI nuclear stain (blue). MLC2v-positive cells were identified by their expression of the red fluorescent protein, TomRed. Bar represents 40 μm.

ventricles are affected. These results are consistent with the recent discovery of left ventricle-dominant and biventricular forms of human ARVC that are primarily associated with desmoplakin mutations (23,24,41). Furthermore, findings from a human patient harboring a recessive desmoplakin mutation that results in loss of desmoplakin, which mimics the loss of desmoplakin in our DSP-cKO model, was shown to lead to a form of ARVC impacting both right and left ventricles (13).

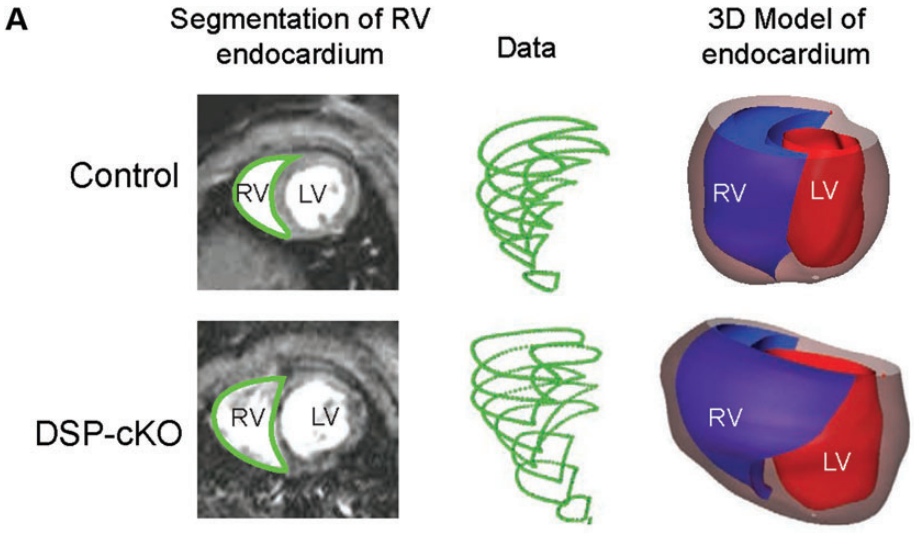

	Control (n = 5)	DSP-cKO (n = 6)
BW (g)	24 ± 2.5	27.5 ± 3
HR (bpm)	533 ± 49	493 ± 47
RV EDV (μl)	45.8 ± 2.6	84.4 ± 6**
RV ESV (μl)	27 ± 2.3	70.2 ± 6**
RV EF (%)	41.2 ± 2	17 ± 1.4**
LV EDV (μl)	42.8 ± 2.2	87.6 ± 3.6**
LV ESV (μl)	19.4 ± 1.9	70 ± 3.7**
LV EF (%)	54.8 ± 2.2	19.8 ± 1.6**
RV wThick. (mm)	0.52± 0.04	0.44 ± 0.08*
LV wThick. (mm)	0.97 ± 0.12	0.80 ± 0.14*

Figure 4. Magnetic resonance image (MRI) analysis of DSP-cKO mice. (**A**) Representative MRIs (short axis) of hearts from control and DSP-cKO mice at 8 weeks. Serial short-axis images were used to generate the 3D geometric model of the endocardium. (**B**) Representative MRIs (long axis) of the hearts from control and DSP-cKO mice at 8 weeks. (**C**) Table denotes measurements obtained from MRI analysis. BW indicates body weight; HR, heart rate; EDV, end-diastolic volume; ESV, end-systolic volume; EF, ejection fraction; and wThick, wall thickness. $^{*}P < 0.05$, $^{**}P < 0.01$.

DSP-cKO hearts exhibit ventricular arrhythmias that can be exacerbated with exercise and catecholamine stimulation

As ventricular arrhythmias are the leading cause of death in ARVC patients, we examined whether conduction defects might account for the sudden death exhibited by DSP-cKO mice. Surface ECG analysis performed on anesthetized DSP-cKO mice showed that they displayed no significant differences in heart rates (control: 446 $\pm$ 23 ($n = 4$) versus DSP-cKO: 478 $\pm$ 50 ($n = 3$) bpm) and PR intervals (Fig. 5A) when compared with littermate control mice. However, significantly increased QRS intervals were observed in DSP-cKO mice when compared with littermate controls, suggestive of ventricular depolarization delay (Fig. 5A). ECG tracings from DSP-cKO mice also revealed spontaneous ectopic premature ventricular contractions (PVC) that were not present in littermate control mice (Fig. 5B). To more closely examine the origin of the spontaneous PVCs, we performed optical mapping on DSP-cKO and littermate control hearts. Langendorff-perfused hearts were mapped while spontaneously depolarizing. Optical maps from control hearts revealed an action potential propagation pattern consistent with fast conduction through the Purkinje network [Fig. 5C (left panel)]. However, DSP-cKO mice revealed spontaneous ectopic multifocal premature beats originating from either the left (Fig. 5C [middle panel)] or right [Fig. 5C (right panel)] ventricles, consistent with the observed PVCs in DSP-cKO hearts *in vivo*. Exercise-induced catecholamine release is a major trigger that has been linked to the onset of ventricular arrhythmias and sudden death in athletes harboring ARVC (42,43). To determine whether exercise and catecholamine stimulation influence the number of ventricular arrhythmias observed in DSP-cKO mice, we subjected mice to treadmill exercise in the absence and presence of low and high doses of epinephrine. We show that the numbers of PVC per second were significantly increased in DSP-cKO mice when

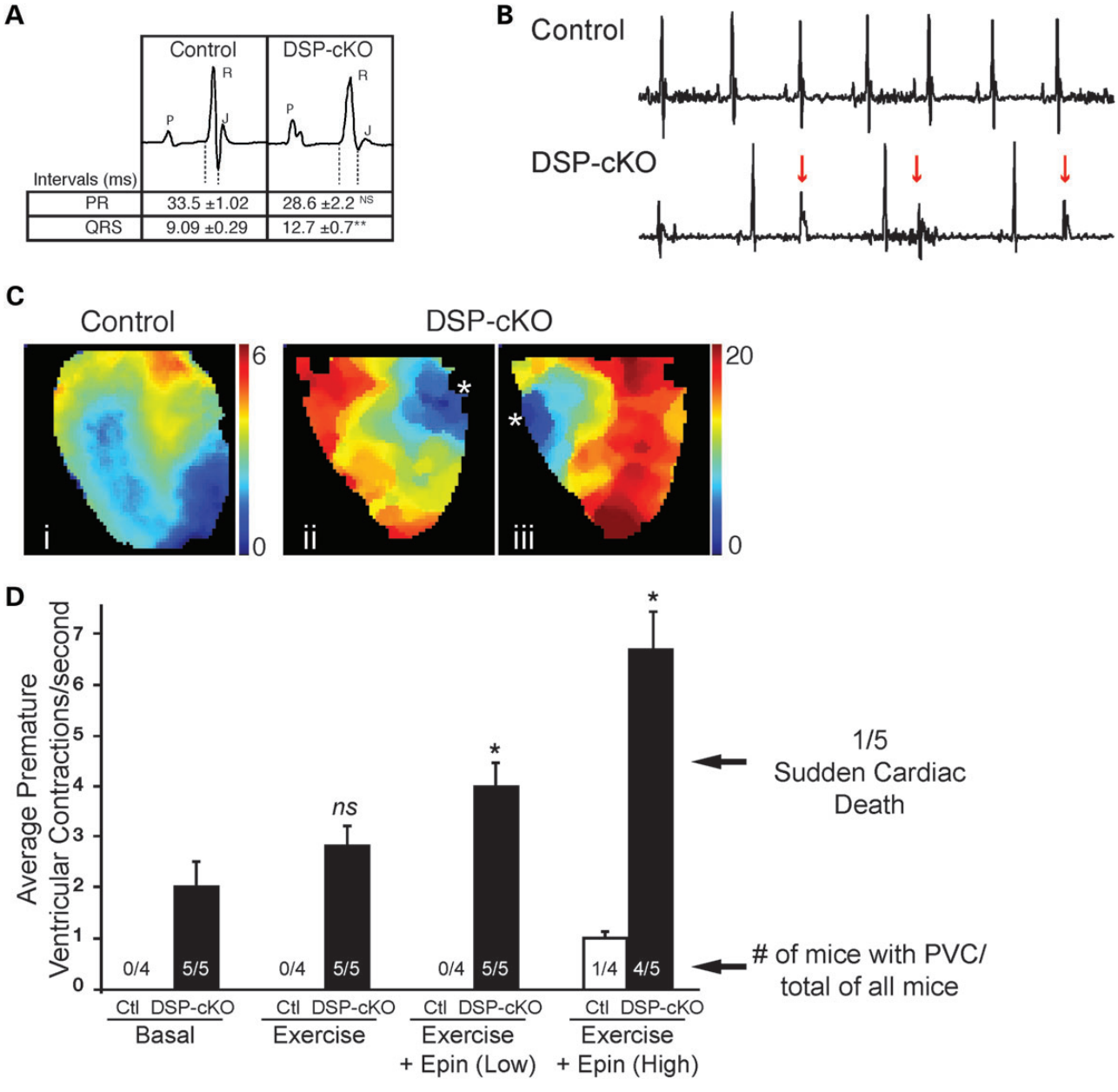

Figure 5. Surface ECG analysis of DSP-cKO mice. (**A**) Representative ECG tracings from control ($n = 6$) and DSP-cKO ($n = 6$) mice at 4 weeks, using Lead II. Mathematical analysis of PR and QRS intervals from the ECG tracings was performed. Data from 100 ECG tracings per mouse were averaged for analysis. QRS duration is indicated by the dotted line. $^{**}P < 0.01$, NS, not significant. (**B**) Representative surface ECG tracings from sedated DSP-cKO and littermate control mice at 4 weeks, using Lead II. Note the PVC (arrows) in DSP-cKO heart. (**C**) Representative optical maps (activation time plots) from non-paced Langendorff-perfused DSP-cKO and littermate control hearts at 6 weeks. Asterisks denote PVC coming from both left and right ventricles within DSP-cKO hearts. Voltage-sensitive dye shows changes in activation time (note scale for control ranges from 0 to 6 ms and scale for DSP-cKO ranges from 0 to 20 ms). (**D**) Analysis of PVC per second in control and DSP-cKO mice at 6 weeks at baseline and with exercise in the absence or presence of low and high doses of epinephrine. $^{*}P < 0.05$.

exposed to exercise and epinephrine stimulation (Fig. 5D). Interestingly, high doses of epinephrine in combination with exercise could also induce sudden cardiac death in DSP-cKO mice that was not observed in littermate controls (Fig. 5D).

DSP-cKO hearts exhibit right ventricular conduction defects associated with loss of connexin 40 expression

Growing evidence points to a key role for anchoring cell–cell junction proteins, such as desmosomes, in cells of the cardiac conduction system (44). Given that loss of desmoplakin leads to ventricular arrhythmias, we sought to examine whether desmoplakin plays a specific role in the ventricular conduction system. Co-staining of cardiac sections with desmoplakin and hyperpolarization-activated cyclic nucleotide-gated cation channel-4 (HCN4), a marker for the cardiac conduction system, in control mice revealed their strong co-localization within the His bundle (HB) and Bundle Branches (RBB and LBB) (Fig. 6A), suggesting that desmoplakin is expressed in cardiomyocytes of the ventricular conduction system. To determine

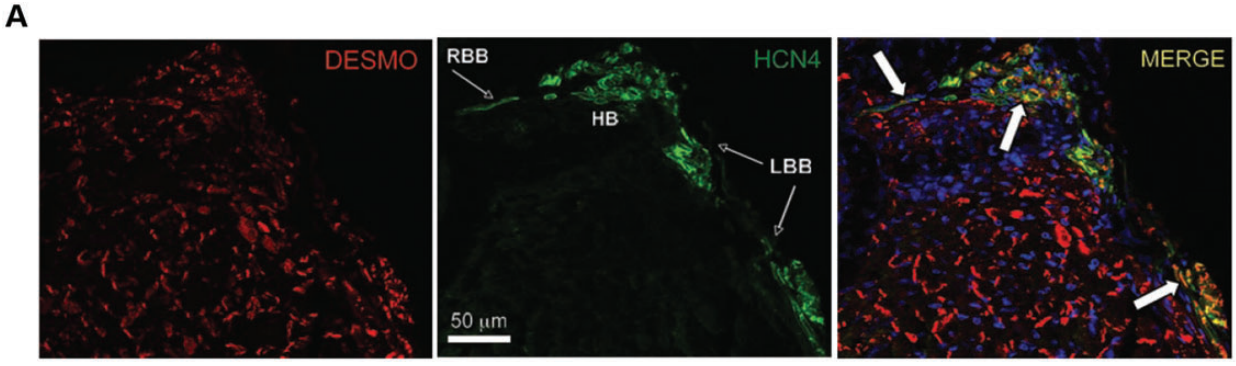

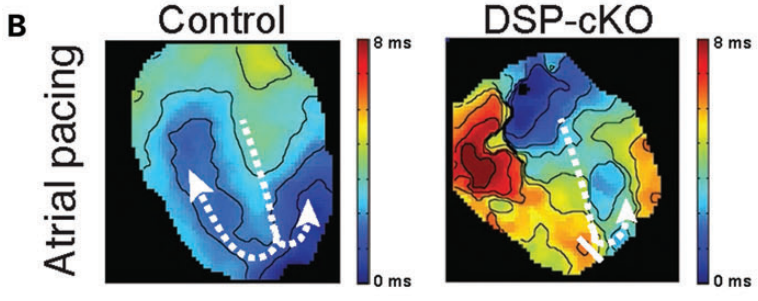

C

	Activation Time	APD20 (ms)	APD50 (ms)	APD80 (ms)	APD80 disp (ms)
Control (n=6)	2.19 ± 0.49	10.53 ± 0.36	20.71 ± 1.83	45.58 ± 9.97	13.76 ± 6.19
DSP-cKO (n=6)	5.24 ± 1.56*	14.09 ± 2.8*	28.16 ± 6.15*	63.95 ± 15.51*	22.55 ± 6.88*

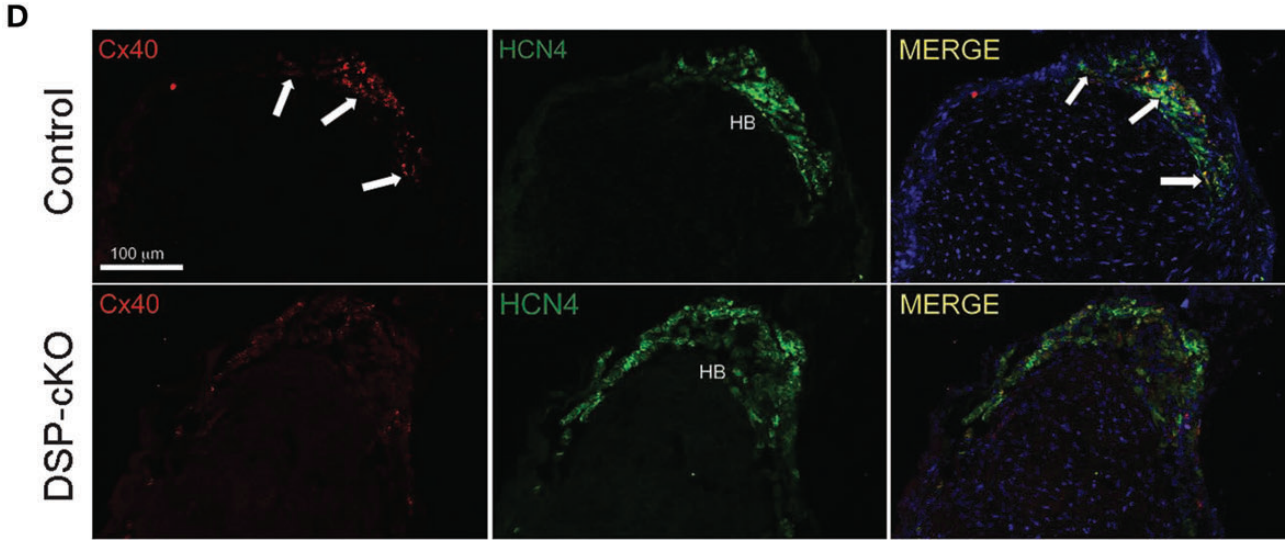

Figure 6. Connexin 40 expression in the ventricular conduction system of DSP-cKO hearts and whole-heart optical mapping analysis of DSP-cKO mice following atrial pacing. (A) Cardiac sections from 3-week-old wild-type mice were co-stained with antibodies against desmoplakin (DESMO, red) and HCN4 (green). Nuclei (blue) were identified through DAPI stain as indicated. Arrows denote doubly stained regions from merged images. Bar represents 50 μm. (B) Activation time plots in control and DSP-cKO hearts following atrial pacing. (C) Summary of activation times, APDs and action potential dispersion in control and DSP-cKO hearts following atrial pacing. $^{*}P < 0.05$. Please note the slowed activation to the RV and increased activation times, APD and APD dispersion in DSP-cKO hearts. (D) Cardiac sections from control (upper panels) and DSP-cKO (lower panels) mice were co-stained with HCN4 (green) and connexin 40 (red). Nuclei (blue) were identified through DAPI. Arrow denotes connexin 40 expression in His bundle (HB) and bundle branch (BB) of WT hearts. Note reduced connexin 40 staining in DSP-cKO heart. Same exposure times were used to detect connexin 40 in control and DSP-cKO hearts. Bar represents 100 μm.

whether loss of desmoplakin has specific functional effects on the ventricular cardiac conduction system, we optically mapped DSP-cKO and littermate control hearts subsequent to atrial pacing. We show that littermate control hearts display rapid action potential depolarization throughout the left and right ventricles following atrial pacing (Fig. 6B). In stark contrast, we show evidence of delayed conduction to the right ventricle in DSP-cKO hearts following atrial pacing, consistent with right bundle branch block (Fig. 6B). Quantitative analyses of action potential propagation in DSP-cKO versus littermate control hearts revealed significantly prolonged activation time, action potential durations (APD20, APD50 and APD80) as well as action potential dispersion (APD80disp) in DSP-cKO hearts when compared with littermate controls (Fig. 6C). These results are consistent with observations in human ARVC patients, who display right ventricular conduction defects, including incomplete or complete right bundle branch block (45). Studies have associated molecular loss of the gap junction protein, connexin 40, with right bundle branch blocks in genetic mouse models (46,47). We show, through co-staining of cardiac sections with connexin 40 and HCN4, that connexin 40 expression is dramatically downregulated in cardiomyocytes of the ventricular conduction system in DSP-cKO hearts, when compared with littermate controls (Fig. 6D). No significant differences in connexin 40 transcript levels could be detected in DSP-cKO versus control hearts, suggesting that the downregulation of Cxn40 is at the post-transcriptional level (Supplementary Material, Fig. S2). These results highlight a direct and important molecular link between desmoplakin and gap junction proteins in the heart and suggest that loss of this connection underlies the right ventricular conduction defects (right bundle branch block) observed in our model.

DSP-cKO hearts exhibit electrical wavefront propagation defects associated with loss of connexin 43 expression

Alterations in geometric patterns of action potential propagation have been associated with arrhythmogenic diseases (48). Thus, to further determine the underlying cause of the ventricular arrhythmias in DSP-cKO hearts, we sought to assess the epicardial pattern of action potential propagation in DSP-cKO versus littermate control hearts, following ventricular epicardial pacing. Optical mapping studies revealed that littermate controls displayed smooth wavefront propagation patterns across the entire epicardium, whereas DSP-cKO hearts displayed pronounced conduction breaks in wavefront propagation within the epicardium

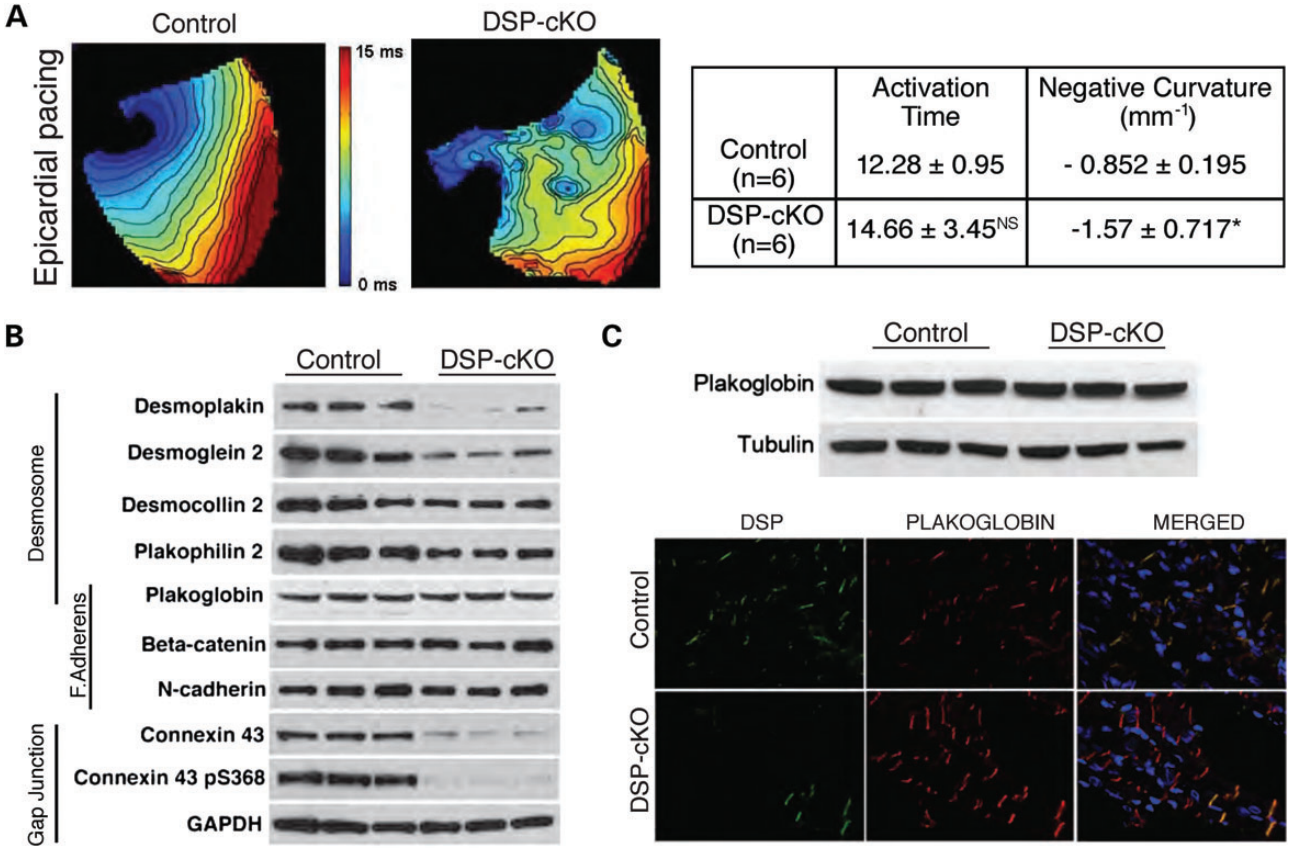

Figure 7. Whole-heart optical mapping analysis of DSP-cKO mice following epicardial pacing and intercalated disc protein expression in DSP-cKO hearts. (A) Representative activation time plots in control and DSP-cKO hearts at 6 weeks following basal posterior epicardial pacing from the right ventricle. Summary of activation times and negative curvature. Please note irregular wavefront pattern and increased negative curvature in DSP-cKO hearts. $^{*}P < 0.05$, NS, non-significant. (B) Protein blot analysis of intercalated disc proteins in total protein extracts from control and DSP-cKO mice at 6 weeks. GAPDH was used as a loading control. (C) Protein blot analysis of plakoglobin in insoluble protein extracts from control and DSP-cKO hearts at 6 weeks and immunofluorescence staining of plakoglobin in cardiac cryosections from control and DSP-cKO mice at 6 weeks. Cryosections were double-labeled with antibodies against desmoplakin (green) and plakoglobin (red), as well as being counterstained with DAPI nuclear stain (blue).

(Fig. 7A). Although no significant differences in overall activation times were observed between mice, we show significant changes in negative wavefront curvature in DSP-cKO versus littermate control hearts (Fig. 7A). These results highlight localized regions of conduction slowing in DSP-cKO hearts that is consistent with a highly arrhythmogenic substrate.

To determine how primary loss of desmoplakin alters the molecular components within the intercalated disc in DSP-cKO hearts, we assessed the expression of desmosomal, fascia adherens and gap junction proteins in whole ventricles from DSP-cKO and littermate control mice at 6 weeks of age (Fig. 7B). A significant 91.2 $\pm$ 7.3% ($n = 3$) reduction in desmoplakin protein expression was observed in DSP-cKO versus control hearts (Fig. 7B). In addition, specific changes in the levels of desmosomal components were observed, which included a significant reduction in desmoglein-2 [70.4 $\pm$ 8.2% ($n = 3$)], desmocollin-2 [56.3 $\pm$ 6.4% ($n = 3$)] and plakophilin-2 [69.7 $\pm$ 4.2% ($n = 3$)] in DSP-cKO whole ventricles compared with controls (Fig. 7B). Interestingly, no significant differences in the levels of fascia adherens proteins, plakoglobin, β-catenin and N-cadherin were observed in DSP-cKO ventricles (Fig. 7B). Reduced levels of plakoglobin at the intercalated disc have been suggested as a common feature in ARVC patients and a potential marker for ARVC (29). To establish whether plakoglobin is lost from the intercalated disc in response to loss of desmoplakin, we specifically assessed the expression level of plakoglobin in the insoluble (intercalated disc-enriched) fractions of DSP-cKO hearts (Fig. 7C) using two independent plakoglobin antibodies. No significant differences in plakoglobin levels were observed in the insoluble protein fractions of DSP-cKO hearts compared with controls (Fig. 7C), similar to what was observed in total protein levels (Fig. 7B). Immunofluorescence staining analyses of cardiac sections further demonstrated that expression of plakoglobin was retained at the intercalated disc with the absence of desmoplakin in DSP-cKO hearts comparable with littermate controls (Fig. 7C), suggesting that the loss of plakoglobin may not be a striking molecular feature of biventricular forms of ARVC resulting from homozygous loss of desmoplakin. Most striking were the effects on gap junctions as significant reductions in levels of connexin 43 [87.2 $\pm$ 4.8% ($n = 3$)] and phosphorylated connexin 43 [S368; 94.3 $\pm$ 5.7% ($n = 3$)] were observed in DSP-cKO ventricles compared with controls (Fig. 7B). Immunofluorescence staining analyses of cardiac sections further affirmed that expression of connexin 43 is downregulated in cardiomyocytes of DSP-cKO hearts when compared with littermate controls (Supplementary Material, Fig. S3). Taken together these results further highlight crosstalk between the desmosomes (desmoplakin) and gap junctions at the intercalated disc in ventricular cardiac muscle that is lost with the loss of desmoplakin in DSP-cKO hearts.

Loss of desmoplakin in neonatal ventricular cardiomyocytes results in primary loss of connexin 43 levels, phosphorylation and function

To establish whether the loss of connexin 43 in DSP-cKO hearts is a primary or secondary consequence of loss of desmoplakin, we evaluated the dose-dependent effects of loss of desmoplakin (AdCre) versus controls (AdlacZ) on key gap junction (connexin 43), desmosomal (plakophilin-2) and fascia adherens (N-cadherin) proteins in neonatal cardiomyocyte cultures generated from DSP-floxed mice (Fig. 8A). We show that the AdCre virus is efficient in causing a dose-dependent reduction in desmoplakin protein expression in neonatal cardiomyocytes, when compared with AdLacZ controls (Fig. 8B). Western blot analysis further demonstrated that a dramatic downregulation of total and phosphorylated (S368) connexin 43 protein levels is observed with the loss of desmoplakin in cardiomyocytes *in vitro* (Fig. 8B), consistent with the reduction found in whole hearts from DSP-cKO mice (Fig. 7B). We further show that the level of downregulation in total and phosphorylated connexin 43 (i) follows the dose-dependent knock-down of desmoplakin in cardiomyocytes and (ii) is found independent of any molecular dissociation of the desmosomal and fascia adherens junction complex, as evidenced by the robust levels of plakophilin-2 and N-cadherin in neonatal cardiomyocytes following desmoplakin knock-down (Fig. 8B). These results suggest that loss of desmoplakin has primary consequences on connexin 43 levels and the gap junction complex.

To determine the functional consequences of primary loss of desmoplakin levels on cardiomyocyte conduction, we optically mapped cardiac action potential propagation in aligned neonatal control (AdlacZ) and desmoplakin-deficient (AdCre) mouse ventricular myocyte cultures (Fig. 8C) (49–51). Activation maps from cardiomyocyte cultures were evaluated for area and distance of action potential propagation along different paths (longitudinal, transverse and arbitrary angle) from the pacing electrode (Fig. 8D). Representative optical maps from AdCre- and AdLacZ-infected cardiomyocytes indicate that both the total area and distance of linear action potential propagation prior to conduction block are markedly less in desmoplakin-deficient versus control cardiomyocytes (Fig. 8E). Quantitative analyses of the distance of continuous propagation in both groups revealed that desmoplakin-deficient cardiomyocytes display significantly reduced distances of continuous propagation across longitudinal, transverse and arbitrary angles when compared with control cardiomyocytes (Fig. 8F). Similarly, desmoplakin-deficient cardiomyocytes displayed significantly reduced areas of continuous propagation compared with control cells, indicative of an increased incidence of conduction block in confluent monolayers (Fig. 8G), suggesting that loss of desmoplakin has a direct impact on cardiac conduction, consistent with loss of connexin 43 function in a setting independent of fibro-fatty manifestation associated with ARVC (Fig. 9).

DISCUSSION

The classic view of ARVC is that it is a right ventricular cardiomyopathy with left ventricular involvement being more secondary with disease progression (28,52). However, more recent long-term follow-up studies of ARVC patients and family members via comprehensive ECG and CMR imaging have identified complex and heterogeneous disease patterns for ARVC, which include left ventricle-dominant and biventricular forms of the disease (20). In addition, recent studies have linked mutations in the desmosomal protein, desmoplakin, to patients primarily exhibiting left ventricular-dominant and biventricular forms of ARVC (22–24), further suggesting that the mechanisms underlying the pathogenesis of specific ARVC subtypes may be dependent on the desmosomal mutation carried by the

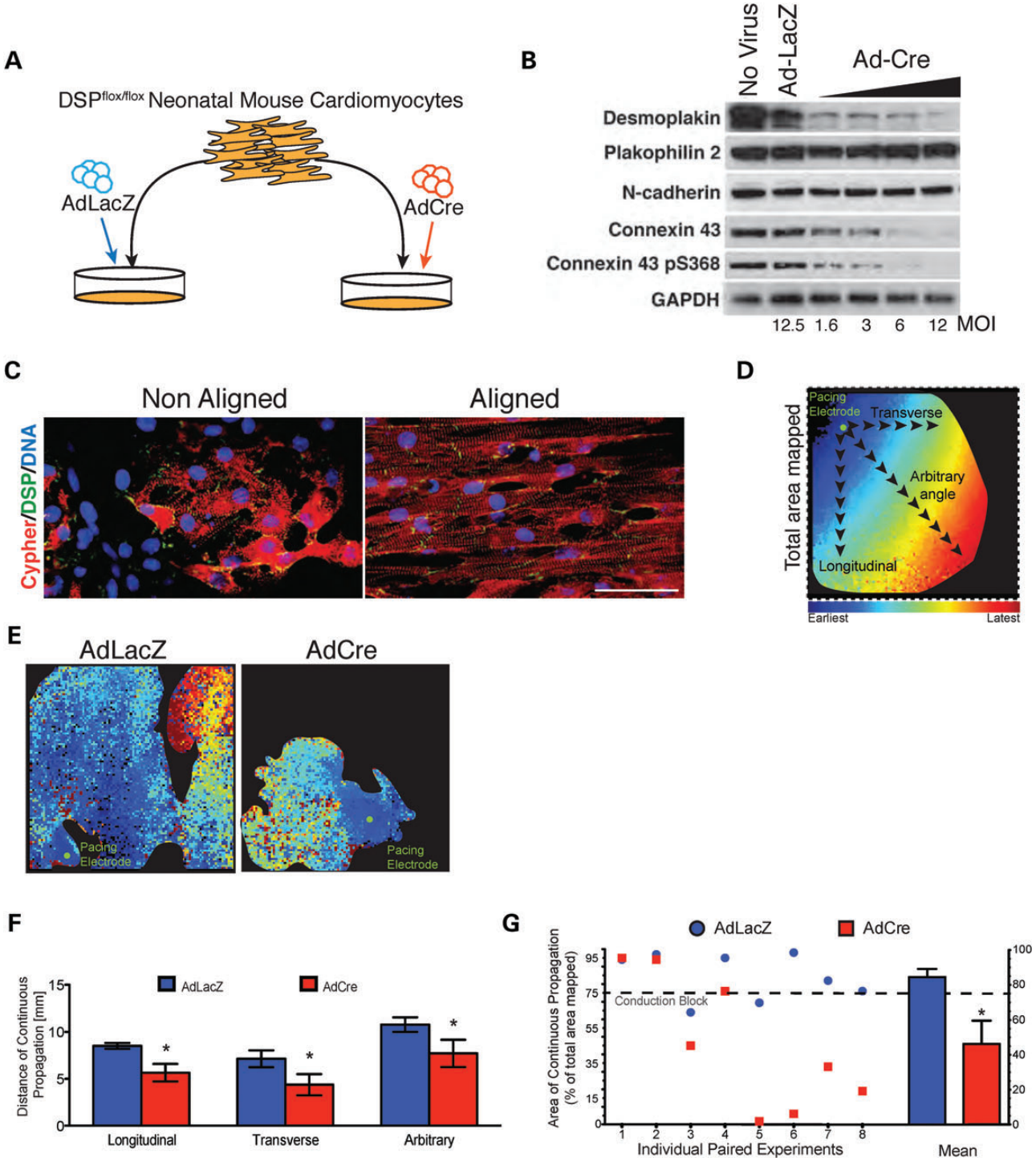

Figure 8. Desmoplakin knock-down leads to electrical conduction block in aligned neonatal mouse ventricular cardiomyocytes (NMVC). (**A**) Schematic representation of the strategy used to knock-down desmoplakin expression in NMVC isolated from $DSP^{flox/flox}$ mice. (**B**) Western blot analysis of intercalated disc protein levels in viral infected cells was performed 4 days post-infection. GAPDH was used as a loading control. (**C**) Immunofluorescence staining of desmoplakin in non-aligned and aligned NVMC. NVMC were double-labeled with antibodies against desmoplakin (green) and cypher (red), as well as counterstained with DAPI nuclear stain (blue). Bar represents 40 μm. (**D**) Distances of continuous propagation were measured at longitudinal and transverse angles as well as at an arbitrary angle across the longest distance. (**E**) Representative activation time plots from control (AdLacZ) and desmoplakin-deficient (AdCre) NVMC 4 days post-infection. Distances of continuous propagation were measured at longitudinal and transverse angles as well as at an arbitrary angle across the longest distance. (**F**) Quantification of distances of continuous propagation in control and desmoplakin-deficient NVMC. $n = 8$, $^*P < 0.05$. (**G**) Quantification of the area of continuous propagation in control and desmoplakin-deficient NVMC. $n = 8$, $^*P < 0.05$. An area of continuous propagation of $<75\%$ of the total area mapped was demonstrative of conduction block.

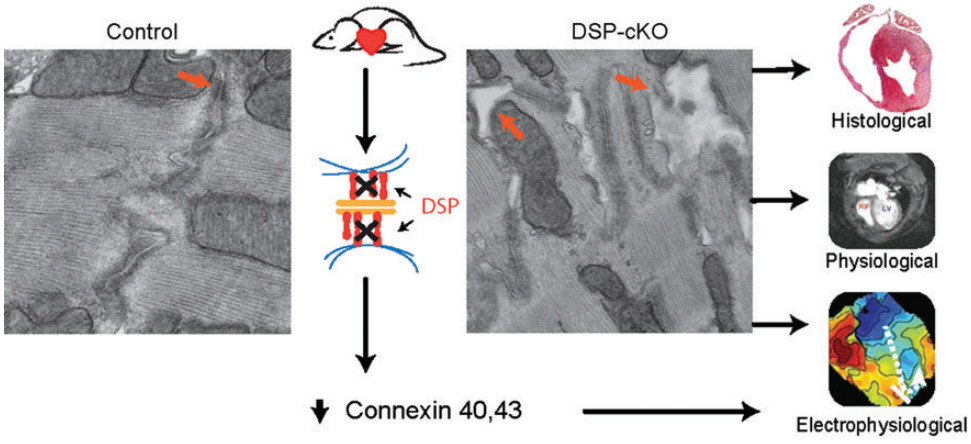

Figure 9. Working model for how cardiomyocyte-specific loss of desmoplakin in DSP-cKO mice leads to disease features reminiscent of a biventricular form of human ARVC. Loss of desmoplakin induces ultrastructural defects at the desmosome that elicit biventricular histological, physiological and electrophysiological defects. Electrophysiological defects also occur independent of structural changes at the desmosome, with loss of desmoplakin directly influencing the levels and function of gap junction proteins.

patient. We provide evidence of a novel mouse model of ARVC (DSP-cKO) resulting from homozygous loss of desmoplakin in cardiomyocytes, which recapitulates the postnatal disease features of a biventricular form of ARVC. By exploiting MRI and 3D reconstruction methods, we have been able to accurately depict the extensive morphological remodeling that occurs in DSP-cKO hearts and show that loss of desmoplakin leads to dramatic changes in both right and left ventricular volumes and function resulting in heart failure and premature death. Most importantly, our mouse model recapitulates findings in a pediatric patient harboring a homozygous loss-of-function mutation in desmoplakin, which was shown to lead to a complete loss of the major isoform of desmoplakin in the heart, resulting in the postnatal onset of a severe biventricular form of ARVC, also resulting in heart failure and premature death (13), thus mimicking the postnatal severity and pathogenic hallmarks as seen in these patients.

The homozygous DSP-cKO mouse model further displays features that broadly fit major criteria proposed by the Taskforce for Diagnosis of Classic Right Dominant Human ARVC (53). Specific features related to these criteria include the appearance of fibro-fatty replacement within the right ventricular free-wall and QRS prolongation. However, we also show increased susceptibility to exercise and catecholamine-induced arrhythmias in DSP-cKO mice, suggesting that exercise can exacerbate the ARVC phenotype, closely mimicking the fact that ARVC is a common cause of sudden death associated with exertion in young athletes (54). Through the development of this novel model of biventricular ARVC, we now have the ability to uncover postnatal mechanisms that are common and unique to the classic RV dominant form of ARVC but also highlight the need to broaden task force criteria to encompass features of left-dominant and biventricular forms of ARVC.

Recent efforts have focused on understanding the molecular and cellular mechanisms underlying the development of fibro-fatty tissue replacement in ARVC. We demonstrate using MLC2v-Cre and the Tomato Red reporter line that DSP-cKO hearts harbor subepicardial fat deposition that originates from a cardiomyocyte lineage, highlighting the propensity of cardiac progenitor cells to transdifferentiate into adipocytes within our ARVC model. These results support previous studies suggesting differentiation of cardiac progenitors into adipocytes in ARVC (25,26) but are likely independent of a mechanism that involves a switch to adipogenesis because of suppressed canonical Wnt/β-catenin signaling as a result of junctional loss and nuclear translocation of plakoglobin (7,25), because no junctional loss or differences in levels of plakoglobin were observed in our DSP-cKO hearts versus littermate control hearts. The predominant and unique fatty deposition at the subepicardium in our ARVC model, which is similar to what is observed in ARVC patients (27), suggests that signals evoked to the subepicardium may be important to consider when understanding mechanisms regulating myocardial fat accumulation. Recent studies suggest that the epicardium has the capacity to signal to adjacent cardiac muscle during development and in the setting of injury that these cells have the capacity to replenish lost cardiomyocytes by contributing to multiple non-cardiac muscle cell types repopulating the infarcted heart (55,56). Thus, future studies directed at understanding whether these signals are affected in ARVC may help propel the field in understanding the mechanisms underlying the fatty deposition associated with ARVC.

The discovery that homozygous loss of desmoplakin leads to a biventricular form of ARVC encompassing ventricular arrhythmias and conduction defects in the absence of loss of junctional plakoglobin, at stages similar to and after the appearance of fibro-fatty replacement further suggests that these mechanisms do not play a pivotal causal role in the pathogenesis of ARVC in our model. Independent studies suggest that suppressed canonical Wnt/β-catenin signaling is also not a feature in mice deficient in plakoglobin that develop a biventricular form of ARVC with spontaneous ventricular arrhythmias and slow conductivity occurring with disease progression (9), suggesting that signaling pathways associated with loss of junctional plakoglobin may not be a predominant feature of left and biventricular forms of ARVC. In support of this, recent studies in humans suggest that not all ARVC patients display loss of junctional plakoglobin (30); thus, future studies determining whether there are distinct

molecular hallmarks for biventricular and left-dominant forms of ARVC in humans may expand our diagnostic criteria and therapies for human ARVC.

Aberrant expression and distribution of connexin 43 referred to as gap junction remodeling has been identified as a common feature of ARVC (29) and may adversely affect cardiomyocyte electrical coupling and contribute to conduction defects and slowing observed in ARVC. However, the molecular mechanisms underlying electrical uncoupling and the development of conduction abnormalities remain poorly understood. Our studies highlight a direct link between desmosomal protein deficiency and connexin remodeling, which may explain the varying clinical presentation of ARVC. We show that the downregulation of connexin 43 is not because of the massive loss of cardiomyocytes as we show that there is specific downregulation of connexin 43 in cardiomyocytes of DSP-cKO hearts. These studies are reinforced as we show that a dose-dependent loss of desmoplakin has direct mechanistic consequences on connexin 43 levels and phosphorylation, leading to conduction abnormalities prior to the molecular dissociation of the mechanical junction complex in a system independent of the fibro-fatty manifestation observed in ARVC. These findings suggest that the histological (fibro-fatty replacement) changes are not necessary to generate an arrhythmogenic substrate but highlight a molecular trigger that may be important for arrhythmias observed in the concealed phase of ARVC. We further show that apoptotic cell death is a contributing factor to the massive increase in collagen deposition observed in DSP-cKO hearts and that these combined histological defects could potentially contribute to worsening of arrhythmias in ARVC, as evidenced by the pronounced conduction breaks in wavefront propagation in DSP-cKO hearts harboring fibro-fatty deposition. Furthermore, we highlight a novel link between desmoplakin and gap junction remodeling at the post-transcriptional level in the ventricular cardiac conduction system, as we show that the loss of connexin 40 protein may underlie the ventricular conduction defects (right bundle branch block) observed in our ARVC model. These studies support recent findings of connexin defects in ARVC patients (57), while extending previous findings that suggest that electrophysiological abnormalities associated with reduced connexin 43 may appear prior to fibro-fatty replacement in the myocardium of human ARVC patients carrying desmoplakin mutations and heterozygous desmoplakin-deficient mice (19). This notion of molecular crosstalk between desmosomal and gap junction proteins has been supported by previous studies that demonstrate that connexin 43 can coexist in macromolecular complexes with desmosomal proteins, such as plakophilin-2 and desmocollin-2a (58,59). Furthermore, desmosomal deficiencies via ARVC causing mutations or loss-of-function studies were shown to abolish this crosstalk (58,59). Our studies also suggest that posttranslational modifications in connexin 43 at S368 are dramatically affected with desmoplakin deficiency. Although the biological significance of this phosphorylation site remains to be determined, previous studies have linked the loss of connexin 43 (S368) phosphorylation and signaling to reduced conduction velocity and resulting ventricular arrhythmias in isolated rat hearts (60), which suggests the possibility that it could be an important contributor to the arrhythmias observed in our ARVC model. Thus, future studies aimed at identifying domains and phosphorylation sites within connexin 43 that mediate this crosstalk could allow for early detection of ARVC prior to the loss of connexins and the occurrence of structural remodeling at the desmosome.

In summary, we present a novel mouse model that is reminiscent of the postnatal onset of a biventricular form of human ARVC at the histological, physiological and electrophysiological levels, as well as highlight underlying molecular changes that directly contribute to the observed electrophysiological abnormalities. The DSP-cKO model has the potential to serve as an invaluable tool for understanding the molecular mechanisms underlying ARVC subclasses, and identifying new diagnostic markers and therapeutic targets for ARVC.

MATERIALS AND METHODS

Generation of cardiomyocyte-specific desmoplakin knockout mouse lines

Desmoplakin-floxed ($Dsp^{flox/flox}$) mice (kind gift from Dr. Elaine Fuchs, Rockefeller University) and heterozygous ventricular myosin light chain-2 Cre [$MLC2v^{(cre+)}$] mice (kind gift from Dr. Ju Chen, University of California-San Diego) have been previously characterized (34,61) and were used to generate cardiomyocyte-specific desmoplakin knockout (DSP-cKO) mice, as shown in Figure 1A. DSP-cKO mice and their control littermates were kept in a congenic C56Bl/6 background. Survival of DSP-cKO mice ($n = 15$) and their control littermates ($n = 15$) was calculated using a Kaplan–Meier survival curve. For fat lineage tracing studies, $DSP^{flox/flox}$:$MLC2v^{(cre+)}$ mice were crossed with a well-established Ai14 heterozygous reporter (strain: B6;129S6-*Gt(ROSA)26Sor*$^{tm14(CAG-tdTomato/Hze/}$) mouse line (Jackson Laboratory, USA) (38), as illustrated in Figure 3E. Reporter mice were kept in a mixed genetic background of C56Bl/6 and Black Swiss. All animal procedures were in full compliance with the guidelines approved by the University of California–San Diego Animal Care and Use Committee.

Mouse cardiac myocyte isolation

Ventricular cardiac myocytes were isolated from adult mouse hearts and neonatal (1–2 days old) DSP-floxed mouse hearts as previously described (62,63).

Protein analysis

Total protein was isolated from cardiomyocytes and ventricles as previously described (31). Insoluble (intercalated disc-enriched) protein extracts were isolated from cardiomyocytes and ventricles using the Triton X-100 method as previously described (10). Immunodetection of desmoplakin (mouse, 1:1000, AbD-Serotec), desmoglein-2 (mouse, 1:100, Fitzgerald), desmocollin-2 (rabbit, 1:1000, Fitzgerald), plakophilin-2 (mouse, 1:1000, Fitzgerald), plakoglobin (mouse, 1:1000, Sigma; goat, 1:1000, Santa Cruz Biotechnology), β-catenin (mouse, 1:1000, BIOMOL International), N-cadherin (rabbit, 1:1000, Abcam), connexin 43 (rabbit, 1:1000, Invitrogen), S368 connexin 43 (rabbit, 1:1000, Invitrogen), glyceraldehyde 3-phosphate dehydrogenase (mouse, 1:2000, Santa Cruz Biotechnology) and α-tubulin (mouse, 1:2000, Sigma) was performed as previously described (31).

Immunofluorescence microscopy

Adult heart cryosections and neonatal ventricular cardiomyocytes were fixed in 100% acetone at −20°C and stained with primary antibodies against desmoplakin (mouse, 1:1000, AbD-Serotec), N-cadherin (rabbit, 1:100, Abcam), perilipin (rabbit, 1:100, Cell Signaling), hyperpolarization-activated cyclic nucleotide-gated potassium channel 4 (rat, 1:100, Abcam), connexin 40 (rabbit, 1:100, Invitrogen), Cypher (rabbit, 1:100, kind gift from Ju Chen, UCSD), plakoglobin (mouse, 1:100, Sigma; goat, 1:100, Santa Cruz Biotechnology), connexin 43 (rabbit, 1:100, Invitrogen) and sarcomeric α-actinin (mouse, 1:200, Sigma). Sections and cells were subsequently stained with fluorescently labeled secondary antibodies (1:100, Jackson ImmunoResearch Inc.) and Hoescht nuclear stain in cases where indicated, followed by imaging using confocal microscopy (Olympus FV1000).

Electron microscopy

Cardiac ventricles were processed for electron microscopy, and images were captured with a Zeiss 10 electron microscope as previously described (62).

Histological analysis

Hearts from 3-week-old mice were perfused in relaxation buffer consisting of 100 mM KCl in phosphate-buffered saline followed by perfusion fixation with 4% paraformaldehyde solution and cryopreservation. Whole-heart (8 μM) cryosections were obtained and stained with Masson's trichrome (Sigma–Aldrich, St. Louis, MO, USA) to detect collagen deposition and Oil Red O (Sigma–Aldrich) to detect lipid deposition according to standard procedures.

Magnetic resonance imaging

In vivo MRI cardiac imaging was performed on a 7T horizontal-bore MR scanner. A 1.9-mm custom-built dual quadrature-driven transverse electromagnetic mode coil was used for transmission and reception of the RF signal. High-resolution bright blood MRI experiments were conducted using an ECG-triggered Fast Low Angle SHot (FLASH) Gradient Echo (GE) pulse sequence tailored for murine imaging as previously described (64), and time series averaging was employed with a FOV of 25 mm^2 and data matrix of 128^2 to yield a sub-millimeter spatial resolution. Equatorial frames containing the largest and smallest chamber diameters were selected to define the end-diastolic and end-systolic times, respectively, with a temporal resolution of 5 ms. For MRI image analyses, four two-dimensional (2D) contours were manually planimetered for each heart at end-diastole and end-systole (LV and RV epi and endo) using image analysis software (ImageJ, NIH). Contour areas were calculated, multiplied by the slice thickness and summed together to approximate calibrated volumes. LV mass was obtained by subtracting endocardial from epicardial volumes and scaling by the specific gravity of myocardial tissue (1.055 g/ml). Stroke volume was defined as LVEDV−LVESV whereas ejection fraction was calculated as 100 × SV/LVEDV. Wall thickness was measured directly from the 2D short-axis images. For 3D reconstruction, endocardial and epicardial contours were fitted to prolate spheroidal meshes with 64 volume elements using linear least-squares minimization (39). Wall and chamber volumes were determined from the mesh, and wall volume multiplied by myocardial density gave the wall mass.

Surface ECG

Adult (4 weeks old) mice were anesthetized with 1% isoflurane. Needle electrodes (30 gauge) were inserted subcutaneously into right forearm and left leg. ECG signals were amplified using Warner Instruments DP-304 Differential Amplifier bandpass filtered between 0.1 and 100 Hz. Signal was further filtered through a Quest Scientific HumBug 50/60 Hz Noise Eliminator and digitized at 3000 Hz.

Whole-heart optical mapping

Optical mapping studies were conducted as previously described (65). Briefly, hearts were isolated from 4-week-old mice and Langendorff-perfused with a heated, oxygenated modified Krebs–Henseleit solution. The heart was submersed in heated perfusate in an optical bath chamber, and a volume-conducted ECG was recorded throughout the experiment. The voltage-sensitive dye di-4-ANEPPS (1 mL bolus, 26 μM) was injected into the perfusion line. Two 470-nm wavelength LED lamps illuminated the ventricular epicardium, and fluorescence was passed through a 610-nm long-pass filter, focused with a fast video lens (F/0.95; Navitar) and recorded by a 12-bit charge-coupled device camera (64 × 64 pixels, 950 frames/s, CA-D1–0128T; DALSA). During recording of paced beats, the atrium or ventricle was stimulated epicardially with a unipolar platinum electrode at a constant current (×1.5 threshold) using a digital stimulator (DS8000; WPI). To eliminate motion artifacts, 15 mM of the electromechanical uncoupler 2,3-butanedione monoxime was perfused. Data were analyzed with custom software in MATLAB. Activation time was identified as at the maximum slope of the action potential upstroke, and action potential duration was calculated at the 20, 50 and 80% levels of repolarization (APD20, APD50 and APD80, respectively). Dispersion of repolarization was defined as the standard deviation of action potential duration (APD) values over the entire anterior epicardium. Disorganization of the wavefront during ventricular epicardial pacing was quantified by calculating the curvature of the activation map as previously described (66). A greater negative curvature indicates increased heterogeneous areas of local conduction block.

Telemetry ECG

Conscious telemetry using an implantable wireless transmitter/receiver system (Datasciences/Ponemah) was performed on 4-week-old mice as previously described (65). For all implantation procedures, the mice were anesthetized with ketamine (100 mg/kg)–xylazine (5 mg/kg) and monitored continuously. A radio transmitter (ETA- F20; Datasciences) was inserted subcutaneously at the subscapular thoracic region and secured via sutures to the skin. Two leads were tunneled through the subcutaneous space cranially and caudally. Transmitters were detected by receiver platforms placed directly underneath the animal's cage. The receiver platforms were linked to an immediately

adjacent computer. Dataquest ART 2.0 data acquisition software (Datasciences) was used for digitization of the signal (at a sampling rate of 1000 Hz) and for on-line display of the electrocardiogram as well as for data storage onto a hard disk. Studies were recorded continuously beginning 96 h following recovery from the implantation. Exercise testing was performed on mice as previously described (67). Following treadmill acclimatization, mice were exercised for at least 45 min on a horizontal treadmill at incrementally faster running speeds (from 12 to 40 m/min), until exhaustion defined by the inability to sustain exercise at 34 m/min or greater. At this point, mice received a high (2 mg/kg) or low (0.5 mg/kg) epinephrine dose via intraperitoneal injection.

Adenoviral infection of cardiomyocyte cultures

Adenovirus vectors containing the lacZ (AdLac-Z) and Cre recombinase (AdCre) cDNAs were prepared (UCSD Viral Vector Core) and used at multiplicity of infections 1.6–12.5 pfu/cell. Neonatal ventricular cardiac myocytes isolated from DSP-floxed mice were plated on laminin and infected with AdLacZ and AdCre, 2 days following isolation, as previously described (68), and as illustrated in Figure 8A. Viral particle carrying medium was changed from cells after 24 h, and cells were subsequently maintained in a media consisting of DMEM, M199, 5% fetal bovine serum, 10% horse serum and 1% penicillin/streptomycin/glutamine for the duration of the study. Cardiomyocytes were analyzed 4 days post-infection.

Cardiomyocyte plating on micropatterned substrates for optical mapping

For optical mapping and immunofluorescence microscopy of aligned cells, a microstructured cell culture environment was created to mimic the myocardium, drawing from earlier works in soft photolithography (50,51,69). Briefly, master molds were patterned on silicon wafers using SU-8 2005-negative photoresist (MicroChem Corp., Newton, MA, USA) and a custom designed photomask (Advance Reproductions Corp., North Andover, MA, USA). These molds were treated with (tridecafluoro-1,1,2,2-tetrahydrooctyl)-1-trichlorosilane (United Chemical Technologies, Inc., Bristol, PA, USA) before the first use to ensure a non-adhesive surface. Polydimethylsiloxane (PDMS) cell culture substrates were molded from the masters by spin-coating Sylgard 186 silicone elastomer (Dow Corning Corp., Midland, MI, USA) prepared at a 10 parts base-to-1 part curing agent ratio, degassed and thermoset 30 min at 70 degrees. After continuing thermosetting at room temperature overnight, the microstructured PDMS was removed from the molds and mounted into custom cell culture chambers described previously (49–51). The resulting PDMS cell culture substrates present 10-μm wide troughs separated by 5-μm-high and 10-μm-wide walls. Laminin derived from murine sarcoma basement membrane was adsorbed onto the entire microstructured cell culture surface using 350-nm wavelength radiation for 10 min (Sigma–Aldrich). Neonatal ventricular cardiac myocytes isolated from DSP-floxed mice were plated on these micropatterned substrates and infected with adenoviruses, as described earlier.

Electrical activation was detected in cardiomyocytes using the transmembrane voltage-sensitive fluorescent probe di-8-ANEPPS (Molecular Probes, Life Technologies, Grand Island, NY, USA). Dye was loaded in a solution of 0.1% Puloronic F-127 and 30 μM di-8-ANEPPS in antibiotic-free media for 25 min, before switching to antibiotic- and serum-free media for imaging. A 470-nm wavelength LED was used to excite the di-8-ANEPPS, directed to the cell culture with a dichroic mirror reflecting <500 nm (Omega Optical, Brattleboro, VT, USA). Emitted light was passed through the dichroic and a 610-nm long-pass filter before collection by a MiCAM Ultima-L CMOS camera at 500 frames per second, 100×100 pixels (SciMedia, Costa Mesa, CA, USA). This system adapts methods used in several earlier optical mapping configurations for a novel application (65,70,71). For an observed culture area of 1 cm^2, activation time was mapped according to the time of maximum upstroke rate at each pixel and conduction of the activation front was measured. Cultures were stimulated with a point electrode at either 100- or 300-ms intervals, though spontaneous activation events were not excluded. Cultures in which activation was conducted over $<75\%$ of the area observed were considered to exhibit conduction block. In several cases, the test was repeated on a cell culture paced at several unique locations to differentiate between conduction block and altered excitability. Maximum distances and areas of continuous activation front propagation without functional conduction block were measured in ImageJ (U. S. National Institutes of Health, Bethesda, MD, USA), with attention given to maximum distances with respect to the longitudinal and transverse axes of cell culture and at an arbitrary angle, and maximum conducting area surrounding any initiation site. Of the experiments considered ($n = 8$), one experiment included two replicates each of control (AdLacZ) and desmoplakin knock-down (AdCre) cultures, and two experiments included two AdCre replicates.

Statistical analysis

Data presented in the text and figures are expressed as mean values ± SEM. Significance was evaluated by the two-tailed Student's *t*-test or repeated-measures ANOVA. For Kaplan–Meier survival analysis, significance was evaluated by the log-rank test. $P < 0.05$ was considered statistically significant.

SUPPLEMENTARY MATERIAL

Supplementary Material is available at *HMG* online.

ACKNOWLEDGEMENTS

We thank the Farquhar Laboratory Transmission Electron Microscopy Core Facility (UCSD, La Jolla, CA, USA) for technical assistance with electron microscopy.

Conflict of Interest statement. None declared.

FUNDING

Microscopy work was performed at the University of California–San Diego Neuroscience Microscopy Shared Facility and was supported by a National Institutes of Health grant (P30 NS047101). Optical mapping and MRI studies were supported in part by National Institutes of Health grants (1R01HL105242,

P50GM094503, 5P01HL46345) to A.D.M. and J.H.O. R.C.L. was a recipient of an American Heart Association Postdoctoral Fellowship (11POST7170006). A.C. was a recipient of an American Heart Association Summer Undergraduate Research Fellowship (11UFEL7870036). This work was supported by a National Scientist Development grant from the American Heart Association (0730281N) and National Institute of Health grant (1R01HL095780-01) from the National Heart, Lung and Blood Institute to F.S.

REFERENCES

1. Sen-Chowdhry, S., Morgan, R.D., Chambers, J.C. and McKenna, W.J. (2010) Arrhythmogenic cardiomyopathy: etiology, diagnosis, and treatment. *Annu. Rev. Med.*, **61**, 233–253.
2. McKoy, G., Protonotarios, N., Crosby, A., Tsatsopoulou, A., Anastasakis, A., Coonar, A., Norman, M., Baboonian, C., Jeffery, S. and McKenna, W.J. (2000) Identification of a deletion in plakoglobin in arrhythmogenic right ventricular cardiomyopathy with palmoplantar keratoderma and woolly hair (Naxos disease). *Lancet*, **355**, 2119–2124.
3. Rampazzo, A., Nava, A., Malacrida, S., Beffagna, G., Bauce, B., Rossi, V., Zimbello, R., Simionati, B., Basso, C., Thiene, G. *et al.* (2002) Mutation in human desmoplakin domain binding to plakoglobin causes a dominant form of arrhythmogenic right ventricular cardiomyopathy. *Am. J. Hum. Genet.*, **71**, 1200–1206.
4. Gerull, B., Heuser, A., Wichter, T., Paul, M., Basson, C.T., McDermott, D.A., Lerman, B.B., Markowitz, S.M., Ellinor, P.T., MacRae, C.A. *et al.* (2004) Mutations in the desmosomal protein plakophilin-2 are common in arrhythmogenic right ventricular cardiomyopathy. *Nat. Genet.*, **36**, 1162–1164.
5. Pilichou, K., Nava, A., Basso, C., Beffagna, G., Bauce, B., Lorenzon, A., Frigo, G., Vettori, A., Valente, M., Towbin, J. *et al.* (2006) Mutations in desmoglein-2 gene are associated with arrhythmogenic right ventricular cardiomyopathy. *Circulation*, **113**, 1171–1179.
6. Syrris, P., Ward, D., Evans, A., Asimaki, A., Gandjbakhch, E., Sen-Chowdhry, S. and McKenna, W.J. (2006) Arrhythmogenic right ventricular dysplasia/cardiomyopathy associated with mutations in the desmosomal gene desmocollin-2. *Am. J. Hum. Genet.*, **79**, 978–984.
7. Garcia-Gras, E., Lombardi, R., Giocondo, M.J., Willerson, J.T., Schneider, M.D., Khoury, D.S. and Marian, A.J. (2006) Suppression of canonical Wnt/beta-catenin signaling by nuclear plakoglobin recapitulates phenotype of arrhythmogenic right ventricular cardiomyopathy. *J. Clin. Invest.*, **116**, 2012–2021.
8. Li, J., Swope, D., Raess, N., Cheng, L., Muller, E.J. and Radice, G.L. (2011) Cardiac tissue-restricted deletion of plakoglobin results in progressive cardiomyopathy and activation of {}β-catenin signaling. *Mol. Cell. Biol.*, **31**, 1134–1144.
9. Li, D., Liu, Y., Maruyama, M., Zhu, W., Chen, H., Zhang, W., Reuter, S., Lin, S.F., Haneline, L.S., Field, L.J. *et al.* (2011) Restrictive loss of plakoglobin in cardiomyocytes leads to arrhythmogenic cardiomyopathy. *Hum. Mol. Genet.*, **20**, 4582–4596.
10. Yang, Z., Bowles, N.E., Scherer, S.E., Taylor, M.D., Kearney, D.L., Ge, S., Nadvoretskiy, V.V., DeFreitas, G., Carabello, B., Brandon, L.I. *et al.* (2006) Desmosomal dysfunction due to mutations in desmoplakin causes arrhythmogenic right ventricular dysplasia/cardiomyopathy. *Circ. Res.*, **99**, 646–655.
11. Pilichou, K., Remme, C.A., Basso, C., Campian, M.E., Rizzo, S., Barnett, P., Scicluna, B.P., Bauce, B., van den Hoff, M.J., de Bakker, J.M. *et al.* (2009) Myocyte necrosis underlies progressive myocardial dystrophy in mouse dsg2-related arrhythmogenic right ventricular cardiomyopathy. *J. Exp. Med.*, **206**, 1787–1802.
12. Sheikh, F., Ross, R.S. and Chen, J. (2009) Cell-cell connection to cardiac disease. *Trends Cardiovasc. Med.*, **19**, 182–190.
13. Uzumcu, A., Norgett, E.E., Dindar, A., Uyguner, O., Nisli, K., Kayserili, H., Sahin, S.E., Dupont, E., Severs, N.J., Leigh, I.M. *et al.* (2006) Loss of desmoplakin isoform I causes early onset cardiomyopathy and heart failure in a Naxos-like syndrome. *J. Med. Genet.*, **43**, e5.
14. Al-Owain, M., Wakil, S., Shareef, F., Al-Fatani, A., Hamadah, E., Haider, M., Al-Hindi, H., Awaji, A., Khalifa, O., Baz, B. *et al.* (2011) Novel homozygous mutation in DSP causing skin fragility-woolly hair syndrome: report of a large family and review of the desmoplakin-related phenotypes. *Clin. Genet.*, **80**, 50–58.
15. Norgett, E.E., Hatsell, S.J., Carvajal-Huerta, L., Cabezas, J.C., Common, J., Purkis, P.E., Whittock, N., Leigh, I.M., Stevens, H.P. and Kelsell, D.P. (2000) Recessive mutation in desmoplakin disrupts desmoplakin-intermediate filament interactions and causes dilated cardiomyopathy, woolly hair and keratoderma. *Hum. Mol. Genet.*, **9**, 2761–2766.
16. Alcalai, R., Metzger, S., Rosenheck, S., Meiner, V. and Chajek-Shaul, T. (2003) A recessive mutation in desmoplakin causes arrhythmogenic right ventricular dysplasia, skin disorder, and woolly hair. *J. Am. Coll. Cardiol.*, **42**, 319–327.
17. Gallicano, G.I., Bauer, C. and Fuchs, E. (2001) Rescuing desmoplakin function in extra-embryonic ectoderm reveals the importance of this protein in embryonic heart, neuroepithelium, skin and vasculature. *Development*, **128**, 929–941.
18. Kirchhof, P., Fabritz, L., Zwiener, M., Witt, H., Schafers, M., Zellerhoff, S., Paul, M., Athai, T., Hiller, K.H., Baba, H.A. *et al.* (2006) Age- and training-dependent development of arrhythmogenic right ventricular cardiomyopathy in heterozygous plakoglobin-deficient mice. *Circulation*, **114**, 1799–1806.
19. Gomes, J., Finlay, M., Ahmed, A.K., Ciaccio, E.J., Asimaki, A., Saffitz, J.E., Quarta, G., Nobles, M., Syrris, P., Chaubey, S. *et al.* (2012) Electrophysiological abnormalities precede overt structural changes in arrhythmogenic right ventricular cardiomyopathy due to mutations in desmoplakin – A combined murine and human study. *Eur. Heart J.*, **33**, 1942–1953.
20. Sen-Chowdhry, S., Syrris, P., Ward, D., Asimaki, A., Sevdalis, E. and McKenna, W.J. (2007) Clinical and genetic characterization of families with arrhythmogenic right ventricular dysplasia/cardiomyopathy provides novel insights into patterns of disease expression. *Circulation*, **115**, 1710–1720.
21. Elliott, P., O'Mahony, C., Syrris, P., Evans, A., Rivera Sorensen, C., Sheppard, M.N., Carr-White, G., Pantazis, A. and McKenna, W.J. (2010) Prevalence of desmosomal protein gene mutations in patients with dilated cardiomyopathy. *Circ. Cardiovasc. Genet.*, **3**, 314–322.
22. Corrado, D. and Thiene, G. (2006) Arrhythmogenic right ventricular cardiomyopathy/dysplasia: clinical impact of molecular genetic studies. *Circulation*, **113**, 1634–1637.
23. Norman, M., Simpson, M., Mogensen, J., Shaw, A., Hughes, S., Syrris, P., Sen-Chowdhry, S., Rowland, E., Crosby, A. and McKenna, W.J. (2005) Novel mutation in desmoplakin causes arrhythmogenic left ventricular cardiomyopathy. *Circulation*, **112**, 636–642.
24. Te Riele, A.S., Bhonsale, A., Burt, J.R., Zimmerman, S.L. and Tandri, H. (2012) Genotype-specific pattern of LV involvement in ARVD/C. *JACC Cardiovasc. Imaging*, **5**, 849–851.
25. Lombardi, R., da Graca Cabreira-Hansen, M., Bell, A., Fromm, R.R., Willerson, J.T. and Marian, A.J. (2011) Nuclear plakoglobin is essential for differentiation of cardiac progenitor cells to adipocytes in arrhythmogenic right ventricular cardiomyopathy. *Circ. Res.*, **109**, 1342–1353.
26. Lombardi, R., Dong, J., Rodriguez, G., Bell, A., Leung, T.K., Schwartz, R.J., Willerson, J.T., Brugada, R. and Marian, A.J. (2009) Genetic fate mapping identifies second heart field progenitor cells as a source of adipocytes in arrhythmogenic right ventricular cardiomyopathy. *Circ. Res.*, **104**, 1076–1084.
27. Basso, C. and Thiene, G. (2005) Adipositas cordis, fatty infiltration of the right ventricle, and arrhythmogenic right ventricular cardiomyopathy. Just a matter of fat? *Cardiovasc. Pathol.*, **14**, 37–41.
28. Corrado, D., Basso, C., Thiene, G., McKenna, W.J., Davies, M.J., Fontaliran, F., Nava, A., Silvestri, F., Blomstrom-Lundqvist, C., Wlodarska, E.K. *et al.* (1997) Spectrum of clinicopathologic manifestations of arrhythmogenic right ventricular cardiomyopathy/dysplasia: a multicenter study. *J. Am. Coll. Cardiol.*, **30**, 1512–1520.
29. Asimaki, A., Tandri, H., Huang, H., Halushka, M.K., Gautam, S., Basso, C., Thiene, G., Tsatsopoulou, A., Protonotarios, N., McKenna, W.J. *et al.* (2009) A new diagnostic test for arrhythmogenic right ventricular cardiomyopathy. *N. Engl. J. Med.*, **360**, 1075–1084.
30. Noorman, M., Hakim, S., Kessler, E., Groeneweg, J.A., Cox, M.G., Asimaki, A., van Rijen, H.V., van Stuijvenberg, L., Chkourko, H., van der Heyden, M.A. *et al.* (2013) Remodeling of the cardiac sodium channel, connexin43, and plakoglobin at the intercalated disk in patients with arrhythmogenic cardiomyopathy. *Heart Rhythm*, **10**, 412–419.
31. Sheikh, F., Chen, Y., Liang, X., Hirschy, A., Stenbit, A.E., Gu, Y., Dalton, N.D., Yajima, T., Lu, Y., Knowlton, K.U. *et al.* (2006) alpha-E-catenin inactivation disrupts the cardiomyocyte adherens junction, resulting in

cardiomyopathy and susceptibility to wall rupture. *Circulation*, **114**, 1046–1055.
32. Zhao, T., Huang, X., Han, L., Wang, X., Cheng, H., Zhao, Y., Chen, Q., Chen, J., Cheng, H., Xiao, R. *et al.* (2012) Central role of mitofusin 2 in autophagosome-lysosome fusion in cardiomyocytes. *J. Biol. Chem.*, **287**, 23615–23625.
33. Ashrafian, H., Czibik, G., Bellahcene, M., Aksentijevic, D., Smith, A.C., Mitchell, S.J., Dodd, M.S., Kirwan, J., Byrne, J.J., Ludwig, C. *et al.* (2012) Fumarate is cardioprotective via activation of the Nrf2 antioxidant pathway. *Cell Metab.*, **15**, 361–371.
34. Chen, J., Kubalak, S.W. and Chien, K.R. (1998) Ventricular muscle-restricted targeting of the RXRalpha gene reveals a non-cell-autonomous requirement in cardiac chamber morphogenesis. *Development*, **125**, 1943–1949.
35. Zhou, X., Stuart, A., Dettin, L.E., Rodriguez, G., Hoel, B. and Gallicano, G.I. (2004) Desmoplakin is required for microvascular tube formation in culture. *J. Cell Sci.*, **117**, 3129–3140.
36. Bolling, M.C. and Jonkman, M.F. (2009) Skin and heart: une liaison dangereuse. *Exp. Dermatol.*, **18**, 658–668.
37. Basso, C., Czarnowska, E., Della Barbera, M., Bauce, B., Beffagna, G., Wlodarska, E.K., Pilichou, K., Ramondo, A., Lorenzon, A., Wozniek, O. *et al.* (2006) Ultrastructural evidence of intercalated disc remodelling in arrhythmogenic right ventricular cardiomyopathy: an electron microscopy investigation on endomyocardial biopsies. *Eur. Heart J.*, **27**, 1847–1854.
38. Madisen, L., Zwingman, T.A., Sunkin, S.M., Oh, S.W., Zariwala, H.A., Gu, H., Ng, L.L., Palmiter, R.D., Hawrylycz, M.J., Jones, A.R. *et al.* (2010) A robust and high-throughput Cre reporting and characterization system for the whole mouse brain. *Nat. Neurosci.*, **13**, 133–140.
39. Chuang, J.S., Zemljic-Harpf, A., Ross, R.S., Frank, L.R., McCulloch, A.D. and Omens, J.H. (2010) Determination of three-dimensional ventricular strain distributions in gene-targeted mice using tagged MRI. *Manag. Reson. Med.*, **64**, 1281–1288.
40. Ho, S.Y. and Nihoyannopoulos, P. (2006) Anatomy, echocardiography, and normal right ventricular dimensions. *Heart*, **92(**Suppl 1), i2–13.
41. Sen-Chowdhry, S., Syrris, P., Prasad, S.K., Hughes, S.E., Merrifield, R., Ward, D., Pennell, D.J. and McKenna, W.J. (2008) Left-dominant arrhythmogenic cardiomyopathy: an under-recognized clinical entity. *J. Am. Coll. Cardiol.*, **52**, 2175–2187.
42. Furlanello, F., Bertoldi, A., Dallago, M., Furlanello, C., Fernando, F., Inama, G., Pappone, C. and Chierchia, S. (1998) Cardiac arrest and sudden death in competitive athletes with arrhythmogenic right ventricular dysplasia. *Pacing Clin. Electrophysiol.*, **21**, 331–335.
43. Heidbuchel, H., Hoogsteen, J., Fagard, R., Vanhees, L., Ector, H., Willems, R. and Van Lierde, J. (2003) High prevalence of right ventricular involvement in endurance athletes with ventricular arrhythmias. Role of an electrophysiologic study in risk stratification. *Eur. Heart J.*, **24**, 1473–1480.
44. Mezzano, V. and Sheikh, F. (2012) Cell–cell junction remodeling in the heart: possible role in cardiac conduction system function and arrhythmias? *Life Sci.*, **90**, 313–321.
45. Fontaine, G., Frank, R., Guiraudon, G., Pavie, A., Tereau, Y., Chomette, G. and Grosgogeat, Y. (1984) Significance of intraventricular conduction disorders observed in arrhythmogenic right ventricular dysplasia. *Arch. Mal. Coeur. Vaiss.*, **77**, 872–879.
46. Simon, A.M., Goodenough, D.A. and Paul, D.L. (1998) Mice lacking connexin40 have cardiac conduction abnormalities characteristic of atrioventricular block and bundle branch block. *Curr. Biol.*, **8**, 295–298.
47. Tamaddon, H.S., Vaidya, D., Simon, A.M., Paul, D.L., Jalife, J. and Morley, G.E. (2000) High-resolution optical mapping of the right bundle branch in connexin40 knockout mice reveals slow conduction in the specialized conduction system. *Circ. Res.*, **87**, 929–936.
48. Akar, F.G. and Rosenbaum, D.S. (2003) Transmural electrophysiological heterogeneities underlying arrhythmogenesis in heart failure. *Circ. Res.*, **93**, 638–645.
49. Lee, A.A., Delhaas, T., Waldman, L.K., MacKenna, D.A., Villarreal, F.J. and McCulloch, A.D. (1996) An equibiaxial strain system for cultured cells. *Am. J. Physiol.*, **271**, C1400–C1408.
50. Gopalan, S.M., Flaim, C., Bhatia, S.N., Hoshijima, M., Knoell, R., Chien, K.R., Omens, J.H. and McCulloch, A.D. (2003) Anisotropic stretch-induced hypertrophy in neonatal ventricular myocytes micropatterned on deformable elastomers. *Biotechnol. Bioeng.*, **81**, 578–587.
51. Camelliti, P., Gallagher, J.O., Kohl, P. and McCulloch, A.D. (2006) Micropatterned cell cultures on elastic membranes as an in vitro model of myocardium. *Nat. Protoc.*, **1**, 1379–1391.
52. Basso, C., Corrado, D., Marcus, F.I., Nava, A. and Thiene, G. (2009) Arrhythmogenic right ventricular cardiomyopathy. *Lancet*, **373**, 1289–1300.
53. Marcus, F.I., McKenna, W.J., Sherrill, D., Basso, C., Bauce, B., Bluemke, D.A., Calkins, H., Corrado, D., Cox, M.G., Daubert, J.P. *et al.* (2010) Diagnosis of arrhythmogenic right ventricular cardiomyopathy/dysplasia: proposed modification of the task force criteria. *Circulation*, **121**, 1533–1541.
54. Kaplan, S.R., Gard, J.J., Protonotarios, N., Tsatsopoulou, A., Spiliopoulou, C., Anastasakis, A., Squarcioni, C.P., McKenna, W.J., Thiene, G., Basso, C. *et al.* (2004) Remodeling of myocyte gap junctions in arrhythmogenic right ventricular cardiomyopathy due to a deletion in plakoglobin (Naxos disease). *Heart Rhythm*, **1**, 3–11.
55. van Wijk, B., Gunst, Q.D., Moorman, A.F. and van den Hoff, M.J. (2012) Cardiac regeneration from activated epicardium. *PLoS One*, **7**, e44692.
56. Perez-Pomares, J.M. and de la Pompa, J.L. (2011) Signaling during epicardium and coronary vessel development. *Circ. Res.*, **109**, 1429–1442.
57. Paul, M., Wichter, T., Gerss, J., Arps, V., Schulze-Bahr, E., Robenek, H., Breithardt, G. and Weissen-Plenz, G. (2013) Connexin expression patterns in arrhythmogenic right ventricular cardiomyopathy. *Am. J. Cardiol.*, **111**, 1488–1495.
58. Oxford, E.M., Musa, H., Maass, K., Coombs, W., Taffet, S.M. and Delmar, M. (2007) Connexin43 remodeling caused by inhibition of plakophilin-2 expression in cardiac cells. *Circ. Res.*, **101**, 703–711.
59. Gehmlich, K., Lambiase, P.D., Asimaki, A., Ciaccio, E.J., Ehler, E., Syrris, P., Saffitz, J.E. and McKenna, W.J. (2011) A novel desmocollin-2 mutation reveals insights into the molecular link between desmosomes and gap junctions. *Heart Rhythm*, **8**, 711–718.
60. Zhu, H., Ding, X., Zou, J., Hou, X. and Cao, K. (2012) Impaired N-cadherin-mediated adhesion increases the risk of inducible ventricular arrhythmias in isolated rat hearts. *Scientific Res. Essays*, **7**, 2983–2991.
61. Vasioukhin, V., Bowers, E., Bauer, C., Degenstein, L. and Fuchs, E. (2001) Desmoplakin is essential in epidermal sheet formation. *Nat. Cell Biol.*, **3**, 1076–1085.
62. Sheikh, F., Ouyang, K., Campbell, S.G., Lyon, R.C., Chuang, J., Fitzsimons, D., Tangney, J., Hidalgo, C.G., Chung, C.S., Cheng, H. *et al.* (2012) Mouse and computational models link Mlc2v dephosphorylation to altered myosin kinetics in early cardiac disease. *J. Clin. Invest.*, **122**, 1209–1221.
63. Wollert, K.C., Taga, T., Saito, M., Narazaki, M., Kishimoto, T., Glembotski, C.C., Vernallis, A.B., Heath, J.K., Pennica, D., Wood, W.I. *et al.* (1996) Cardiotrophin-1 activates a distinct form of cardiac muscle cell hypertrophy. Assembly of sarcomeric units in series VIA gp130/leukemia inhibitory factor receptor-dependent pathways. *J. Biol. Chem.*, **271**, 9535–9545.
64. Frahm, J., Haase, A. and Matthaei, D. (1986) Rapid NMR Imaging of Dynamic Processes Using the FLASII Technique. *Magn. Reson. Med.*, **3**, 321–327.
65. Zemljic-Harpf, A.E., Miller, J.C., Henderson, S.A., Wright, A.T., Manso, A.M., Elsherif, L., Dalton, N.D., Thor, A.K., Perkins, G.A., McCulloch, A.D. *et al.* (2007) Cardiac-myocyte-specific excision of the vinculin gene disrupts cellular junctions, causing sudden death or dilated cardiomyopathy. *Mol. Cell Biol.*, **27**, 7522–7537.
66. Gutstein, D.E., Morley, G.E., Vaidya, D., Liu, F., Chen, F.L., Stuhlmann, H. and Fishman, G.I. (2001) Heterogeneous expression of Gap junction channels in the heart leads to conduction defects and ventricular dysfunction. *Circulation*, **104**, 1194–1199.
67. Lehnart, S.E., Mongillo, M., Bellinger, A., Lindegger, N., Chen, B.X., Hsueh, W., Reiken, S., Wronska, A., Drew, L.J., Ward, C.W. *et al.* (2008) Leaky Ca2+ release channel/ryanodine receptor 2 causes seizures and sudden cardiac death in mice. *J. Clin. Invest.*, **118**, 2230–2245.
68. Sheikh, F., Raskin, A., Chu, P.H., Lange, S., Domenighetti, A.A., Zheng, M., Liang, X., Zhang, T., Yajima, T., Gu, Y. *et al.* (2008) An FHL1-containing complex within the cardiomyocyte sarcomere mediates hypertrophic biomechanical stress responses in mice. *J. Clin. Invest.*, **118**, 3870–3880.
69. Camelliti, P., McCulloch, A.D. and Kohl, P. (2005) Microstructured cocultures of cardiac myocytes and fibroblasts: a two-dimensional in vitro model of cardiac tissue. *Microsc Microanal.*, **11**, 249–259.
70. Sung, D., Omens, J.H. and McCulloch, A.D. (2000) Model-based analysis of optically mapped epicardial activation patterns and conduction velocity. *Ann. Biomed. Eng.*, **28**, 1085–1092.
71. Zhang, Y., Sekar, R.B., McCulloch, A.D. and Tung, L. (2008) Cell cultures as models of cardiac mechanoelectric feedback. *Prog. Biophys. Mol. Biol.*, **97**, 367–382.